Supporting Information

Competitive Li-ion Coordination Constructing Three-Dimensional Transport Network for Ultra-High Ionic Conductivity of Composite Solid-State Electrolyte

Yiteng Ma[a,b,d], Yong Qiu[c,d], Ke Yang[a,b]*, Shun Lv[a,b], Yuhang Li[a,b], Xufei An[a,b], Guanyou Xiao[a,b], Zhuo Han[a,b], Yuetao Ma[a,b], Likun Chen[a,b], Danfeng Zhang[a,b], Wei Lv[a], Yun Tian[c]*, Tingzheng Hou[a], Ming Liu[a], Zhen Zhou[c], Feiyu Kang[a,b] and Yan-Bing He[a]*

[a] *Shenzhen All-Solid-State Lithium Battery Electrolyte Engineering Research Center, Institute of Materials Research (IMR), Tsinghua Shenzhen International Graduate School, Shenzhen 518055, China.*

[b] *School of Materials Science and Engineering, Tsinghua University, Beijing 100084, China.*

[c] *Interdisciplinary Research Center for Sustainable Energy Science and Engineering (IRC4SE²), School of Chemical Engineering, Zhengzhou University, Zhengzhou 450001, Henan, China*

[d] *These authors contributed equally: Yiteng Ma, Yong Qiu.*

Correspondence and requests for materials should be addressed to yangk22@mails.tsinghua.edu.cn, ytian009@zzu.edu.cn, he.yanbing@sz.tsinghua.edu.cn

Experimental Sections

Materials.

$C_8H_7NO_4$ (H_2BDC, 98%) and $C_2H_4O_2$ (99.5%) were purchased from Macklin. PAN (M_w=150,000), $HCON(CH_3)_2$ (DMF, 99.9%) and $ZrCl_4$ (99.9%) came from Sigma Aldrich. PVDF (M_w=300,000, kynar 761) came from Arkema. LiFSI (99.99%) was purchased from Tinci Materials Technology Co., Ltd. $LiNi_{0.8}Co_{0.1}Mn_{0.1}O_2$ (NCM811, D_{50}=3.77 μm), polyvinylidene difluoride binder (PVDF5130, M_w=1,200,000Da, particle size: 100 μm, 99.5%), Super P (particle size: 40~50 nm, 99.5%), Al foil (thickness: 10 μm, 99.9%), Cu foil (thickness: 10 μm, 99.9%) and coin cell components (CR2032, spacer: 15.8 × 1 mm, spring: 15.4 × 1.1 mm) were purchased from Guangdong Canrd New Energy Technology Co., Ltd. N-methyl-2-pyrrolidone (NMP, AR) was purchased from Shanghai Aladdin Biochemical Technology Co., Ltd. Li foil (thickness: 450 μm, diameter: 15.6 mm; thickness: 550 μm, diameter: 12.5 mm) came from China Energy Lithium Co., Ltd.

Materials Characterization.

The X-ray diffraction (XRD) measurements of the samples were carried out on a Rigaku Smartlabwith Cu-Kα radiation. The morphologies and structures of the samples were analyzed by a scanning electron microscope (SEM, HITACH S4800) with energy dispersive spectroscopy (EDS) for elemental analysis and a field emission transmission electron microscope (FE-TEM, FEI Tecnai F30). The X-ray photoelectron spectroscopy (XPS) measurement was collected on a PHI 5000 VersaProbe II instrument. All reported binding energy values were calibrated with hydrocarbon C 1s peak at 284.8 eV. The ^{7}Li, ^{19}F and ^{1}H nuclear magnetic resonance (NMR) spectrum of the liquid Li-DMF solution and Li-MOF-DMF suspension were performed with a Bruker 600 MHz AVANCE III spectrometer (Temperature: 303 K; Relaxation Delay: 3 s; Pulse Width: 12 μs; Acquisition Time: 0.2 s; Scans: 1024). The solid-state ^{7}Li and ^{19}F nuclear magnetic resonance (NMR) were performed with a Bruker 400 MHz AVANCE III spectrometer. The atomic force microscope-nano infrared spectroscopy (AFM-nano-IR) measurements were undertaken with Bruker Anasys nanoIR2-fs instrument. The Fourier transform infrared (FTIR) spectra were executed by VERTEX 70 spectrometer in an attenuated total reflection (ATR) mode. Raman spectroscopy was conducted by a Micro-laser confocal Raman spectrometer (Horiba LabRAM HR800, France) at room temperature with a 532 nm laser. The SEI component and 3D distribution were collected by time-off light secondary ion mass spectrometry (ToF-SIMS, PHI nanoTOF II, 30 keV, 2 nA) in a 200 μm (length) × 200 μm (width) × 50 nm (thickness) region after cycling Li‖NCM811 cells 20 times at 1C and 25 °C. The roughness and Young's modulus of the SEI were measured by AFM (Bruker Dimension Ico). The cross-sectional morphologies of the cathodes were collected on focused ion beam-scanning electron microscope (FIB-SEM, FEI Helios G4 UC). The CEI images on the cycled NCM811 were collected by a field emission transmission electron microscope (FE-TEM) FEI Tecnai F30. Thermogravametric analysis (TGA) was performed using a Netzsch STA 449F3 thermal analyzer from

room temperature to 600 ºC at a heating rate of 10 ºC min^{-1} in N$_2$ atmosphere. The ratio of stress to strain was evaluated by the stress-strain curves and the tensile strength was taken as the stress value at the maximum of the curves.

Preparation of h-PAN nanofibers.

The h-PAN nanofibers were prepared via an electrospinning method and following a heat treatment process. In a typical procedure, 1.2 g of PAN powders were dissolved in 15 mL DMF solution by magnetic stirring at room temperature. Then the obtained homogeneous PAN solution was electrospun into h-PAN precursors under the electrospinning voltage of -1~20 kV and pumping rate of 1.2 mL h^{-1}. Subsequently, the precursors were thermally stabilized at 240 ºC for 40 min with the heating rate of 3 ºC min^{-1} to obtain h-PAN nanofibers.

Preparation of h-PAN@MOF networks.

h-PAN@MOF networks were synthesized via the solvothermal strategy[1]. Specifically, 0.294 g of ZrCl$_4$ was dissolved in 50 mL of DMF to obtain solution A, then, 0.228 g of H$_2$BDC was dissolved in 50 mL of DMF to obtain solution B. After that, solution B and 12 ml of acetic acid were added dropwise to solution A to obtain precursor solution. Subsequently, a certain quality of h-PAN nanofibers was completely immersed in the mixed solution. After solvothermal reaction in a Teflon-lined steel autoclave at 120 ºC for 24 h, the obtained h-PAN@MOF networks were taken out and washed with DMF and ethanol for three times, and dried at 70 ºC in vacuum oven for 24 h.

Preparation of PVDF, PP and PPM electrolytes.

PVDF powders were dried at 60 ºC for 12 h before further removal of the trapped water. Self-standing PVDF, PP and PPM electrolytes were prepared by solution casting method with a PVDF/LiFSI weight ratio of 3/2 (400 mg/267 mg) in 6 mL DMF solvent. The h-PAN@MOF networks were immersed in the solution, and placed in a vacuum tank with continuous evacuation for half an hour to remove air bubbles, then the PPM electrolytes were obtained by drying for 8 h at 55 ºC in glass dish (diameter: 90 mm) and stored in glovebox before use. The PP electrolytes were obtained by immersing the h-PAN nanofibers into the solution using the same preparation method as the PPM electrolytes. In addition, the PVDF polymer electrolytes were directly obtained by solution casting method.

Fabrication of cells.

The NCM811 cathode was prepared by following steps. The mixture of 0.8 g (80 wt.%) single crystal NCM811 powders, 0.1 g (10 wt.%) PVDF5130 and 0.1 g (10 wt.%) Super P was manually grinded in an agate mortar for 10 min in an air environment and then dispersed in 2.4 mL NMP by magnetic stirring for 4 h to form a slurry. Then the slurry was casted on an Al foil and dried at 120 °C for 2 h under vacuum. The cathode active material loading is around 1.2 mg cm^{-2}. For high loading cathode, the areal capacity is 0.81 mAh cm^{-2} (4.5 mg cm^{-2}) and 1.62 mAh cm^{-2} (9 mg

cm^{-2}). The CR2032 solid-state Li||NCM811 coin cells were assembled in an Ar-filled glove box (O$_2$ and H$_2$O < 0.1 ppm) without any liquid electrolyte or solvent. The thickness of Li foil is 450 μm and the diameter is 15.6 mm. The diameter of cathode is 12 mm, and the diameter of electrolyte is 19 mm. The Li||Li cells were assembled using two Li foil (thickness: 450 μm, diameter: 15.6 mm; thickness: 550 μm, diameter: 12.5 mm). In the coin cell, 2 spacers and a spring were used. The CR2032 solid-state Li||Cu cells were assembled using a Li foil (thickness: 550 μm, diameter: 12.5 mm), electrolyte (diameter: 19 mm) and a Cu foil (thickness: 10 μm, diameter: 16 mm). During the fabrication and formation process, a proper pressure of 700 kg (4.9 × 10^6 Pa) was applied to ensure excellent interfacial contact of the PPM electrolyte with both the Li metal anode and NCM811cathode.

Electrochemical measurements.

The ionic conductivities were tested by electrochemical impedance spectroscopy (EIS) from 7 MHz to 0.1 Hz with a 20 mV AC oscillation on a VMP3 multichannel electrochemical station (Bio Logic Science Instruments, France). The test cells were assembled by a small piece of electrolyte slice (diameter: 19 mm) sandwiched between two stainless-steel (SS) (thickness: 1 mm; diameter: 16 mm) blocking electrodes. Prior to the EIS measurements, the cells were kept at each test temperature (-30, 30, 40, 50, 60, 70, 80 ºC) for 1 h to reach the thermal equilibrium. The ionic conductivities (σ) were calculated following equation (1):

$$\sigma = \frac{L}{RS}$$
(1)

where L is the thickness of electrolytes, R is obtained by EIS measurement with electrolytes sandwiched between two stainless plates of steel, and S is the area of stainless steel. The activation energy was calculated from the Arrhenius equation (2):

$$\sigma = \sigma_0 \exp\left(-\frac{E_a}{RT}\right)$$
(2)

where σ_0 and E_a is the pre-exponential factor and the activation energy of ions transportation, respectively.

The Li||Li symmetric cells were assembled and polarized by a voltage ($\Delta V = 20$ mV) for 3600 s to test the Li transference number t_{Li^+}. At the same time, EIS measurement as well as initial and steady state of the Li||Li cells was performed from 7 MHz to 0.1 Hz with a 20 mV AC oscillation. t_{Li^+} is calculated following equation (3):

$$t_{Li^+} = \frac{I_s(\Delta V - I_0 R_0)}{I_0(\Delta V - I_s R_s)}$$
(3)

where I_s and I_0 is the steady-state currents and initial current, respectively, R_0 and R_s is the interfacial resistance before and after polarization, respectively.

The linear sweep voltammetry (LSV) curves were examined from 0 to 6 V versus Li/Li$^+$ at a scanning rate of 0.1 mV s^{-1} using a VMP3 multichannel electrochemical station. Stainless-steel blocking electrode was used as the working electrode, while Li foil was used as the counter and the reference electrodes in this system. The stability window values of electrolytes were recorded as the voltage when the current increased to 10 μA. Galvanostatic charge/discharge tests of the cells were performed on LAND CT2001A battery test system and Neware battery test system. The Li‖NCM811 cells were cycled at 0.1C (1C = 180 mA g^{-1}) for the first 3 times before the long-term cycling tests at 1C. The Li‖NCM811 cells were cycled at 0.1C and 0.5C for the first 3 times, respectively, before the long-term cycling tests at 2C. The Li‖NCM811 cells were cycled at 0.1C, 0.5C, 1C and 2C for the first 3 times, respectively, before the long-term cycling tests at 5C. The cycled cells were transferred into a glovebox and dissembled for further examination. The cycled lithium metal anode and NCM811 cathode were transferred into a chamber with a sealed Ar-filled vessel for SEM and XPS examinations.

The Coulombic efficiencies of Li depositing/stripping in different electrolytes were investigated in Li‖Cu coin cells. For the method reported by Zhang et al.,[2] A given amount of areal charge capacity (Q_T, 0.5 mAh cm^{-2}) is used to deposit Li onto the Cu substrate first as a Li reservoir, then a smaller portion of this areal charge capacity (Q_c, 0.1 mAh cm^{-2}) is used to cycle Li between working and counter electrodes under 0.1 mA cm^{-2} for 10 cycles. After 10 cycles, a final exhaustive strip of the remaining Li reservoir is performed to the cut-off voltage of 1 V. The final stripping areal charge capacity (Q_S), corresponding to the quantity of Li remaining after cycling, is measured. The average CE over 10 cycles can be calculated from equation (4):

$$CE_{avg} = \frac{10Q_c + Q_s}{10Q_c + Q_T}$$

(4)

Computational methods.

DFT calculations. The density functional theory (DFT) computations with van der Waals (vdW) corrections were carried out in the Vienna ab initio Simulation Package (VASP)[3]. The Perdew-Burke-Ernzerhof (PBE) functional within the generalized gradient approximation (GGA) was used to describe the exchange-correlation interaction[4]. Projector augmented wave (PAW) methods were used for pseudopotentials[5]. An energy cutoff of 400 eV was adopted for the plane-wave basis set. A vacuum layer of 20 Å was used to prevent the interaction between periodic images. The energy convergence criterion for geometric optimization was set to be 10^{-5} eV. The γ-centered Monkhorst-Pack scheme with a K-point resolution of 0.07 π/Å was used in all DFT computations. The DFT-D3 method was applied to account for the van der Waals interaction[6]. The VASPKIT was utilized for post-processing of computational data[7].

The adsorption energy (E$_{ads}$) was calculated according to the equation below,

$$E_{ads} = E_{12} - E_1 - E_2 \qquad (5)$$

5

where E_{12} is the optimized total energy of the adsorbed structure, and E_1, E_2 are the optimized energies of the adsorbate and adsorbent.

MD simulations. All molecular dynamic simulations were carried out with the LAMMPS (Large Scale Atomic/Molecular Massively Parallel Simulator) package[8], with electrolyte molar ratios taken from corresponding experimental values. The Universal Force Field (UFF)[9] and Optimized Potentials for Liquid Simulations all atom (OPLS-AA) force fields were adopted for MOF and solvent[10-12]. The force field parameters for Li^+ and FSI^- are taken from Jensen et al[13] and Canongia et al[14]. Charges of the solvent molecule were fitted from first principle calculations using the RESP method[15] analyzed by multiwfn[16], with B3LYP/def2TZVP level of theory[17]. The charges of MOF (UiO-66-NH_2) were obtained using the REPEAT charge fitting method[18]. The model assembly is performed using Packmol[19] and Moltemplate[20].

The simulation procedure for the bulk electrolyte consists of an energy minimization using the steepest descent method followed by a 2 ns equilibration step using a Berendsen barostat and a 20 ns production run using a Parrinello–Rahman barostat, both at a reference pressure of 1 bar. A Nosé–Hoover thermostat was used throughout with a reference temperature of 298 K. The particle mesh Ewald method was used to calculate electrostatic interactions, with a real-space cut-off of 0.12 nm and a Fourier spacing of 0.12 nm. A cut-off of 0.12 nm was used for non-bonded Lennard-Jones interactions. Periodic boundary conditions were applied in all directions. Convergence of the system energy, temperature and box size were checked to verify equilibration. The final 5 ns of the production run were used to generate RDFs results.

To investigate the interfacial impact of UiO-66-NH_2 on ion migration, the UiO-66-NH_2 interface thickness was approximately 2.1 nm to ensure the absence of any non-physical interactions between the liquid electrolytes on both sides of the UiO-66-NH_2. The solvent concentration on both sides of the interface remained consistent. The stability of the UiO-66-NH_2 structure was observed. For the interface simulation, the system was incompressible in the x and y directions but allowed compression in the z direction (perpendicular to the interface).

Supplementary Figures
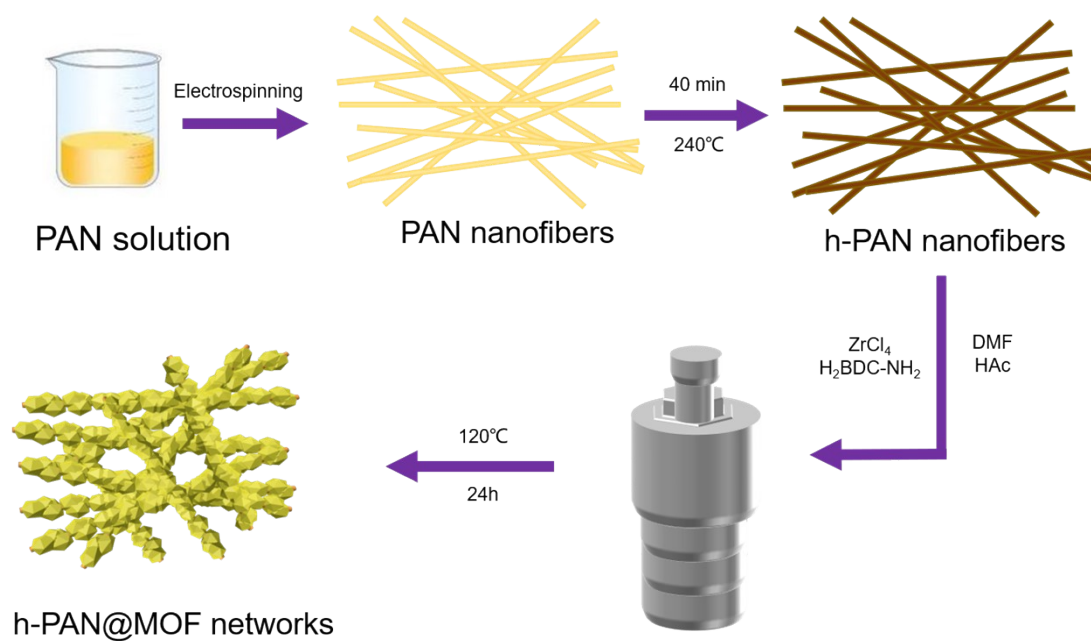
Fig. S1. Schematic diagram for the fabrication of h-PAN@MOF networks.
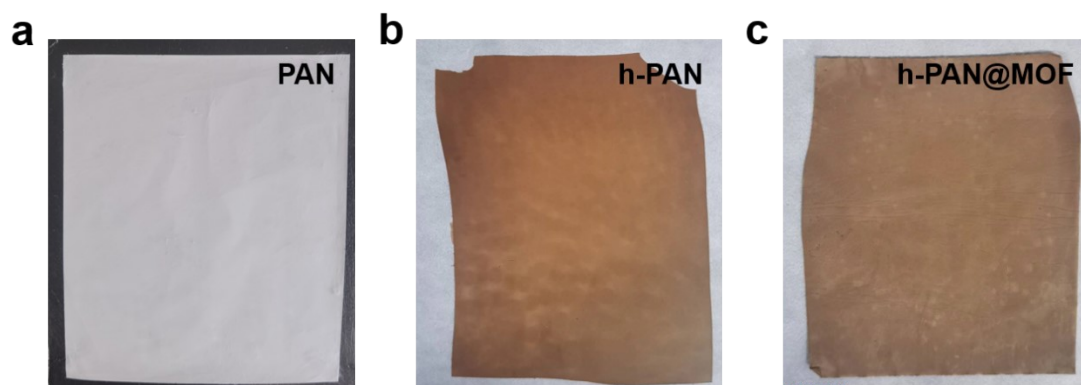
Fig. S2. Optical photographs of (a) PAN nanofibers, (b) h-PAN nanofibers and (c) h-PAN@MOF networks.
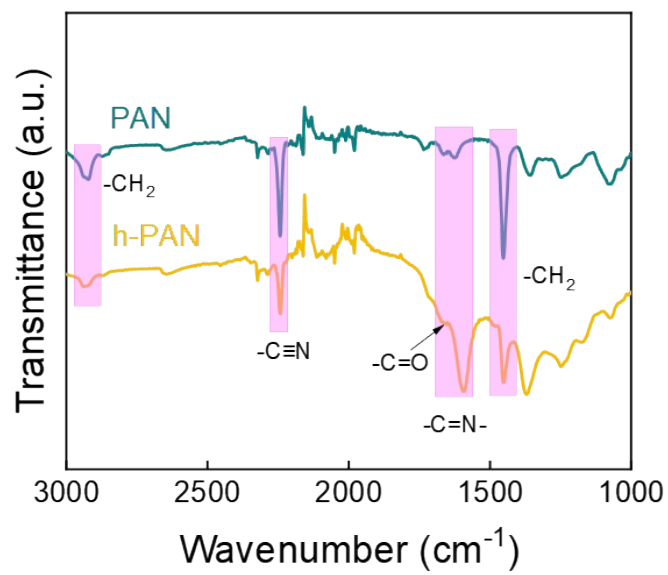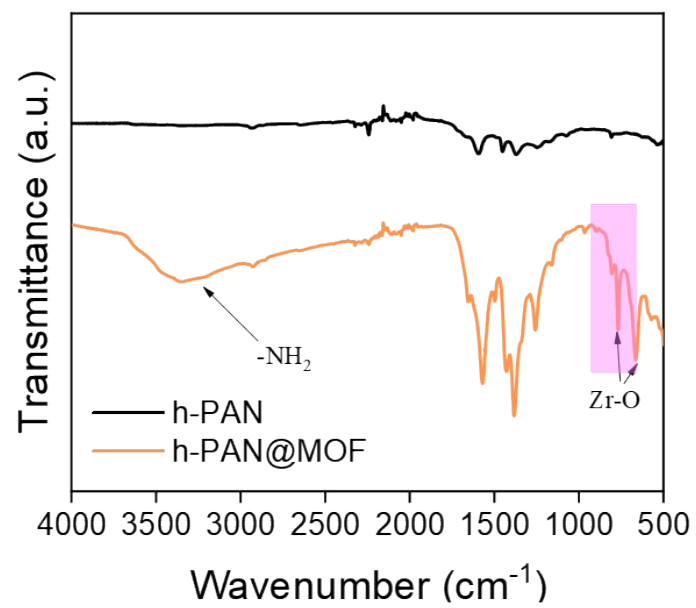
Fig. S3. FTIR spectra of PAN and h-PAN nanofibers.

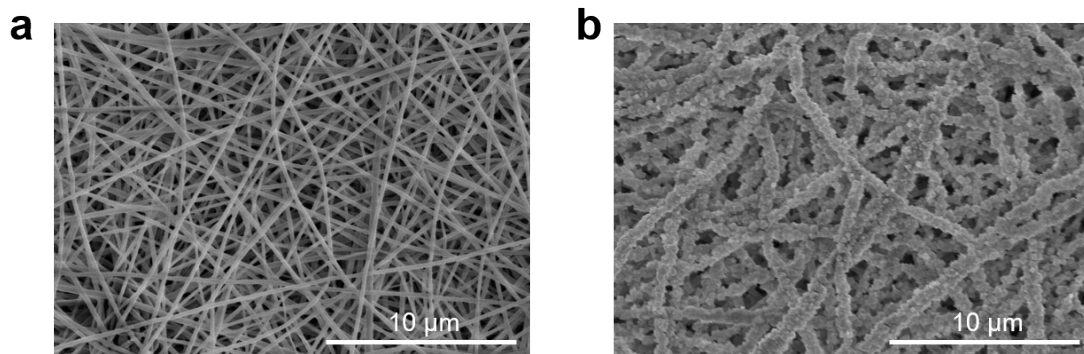**Fig. S4.** FTIR spectra of h-PAN nanofibers and h-PAN@MOF networks.

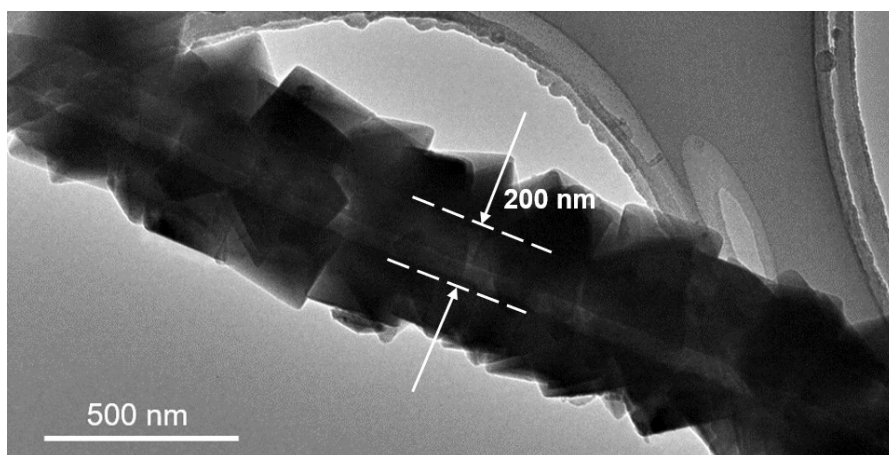**Fig. S5.** SEM images of (a) h-PAN nanofibers and (b) h-PAN@MOF networks.
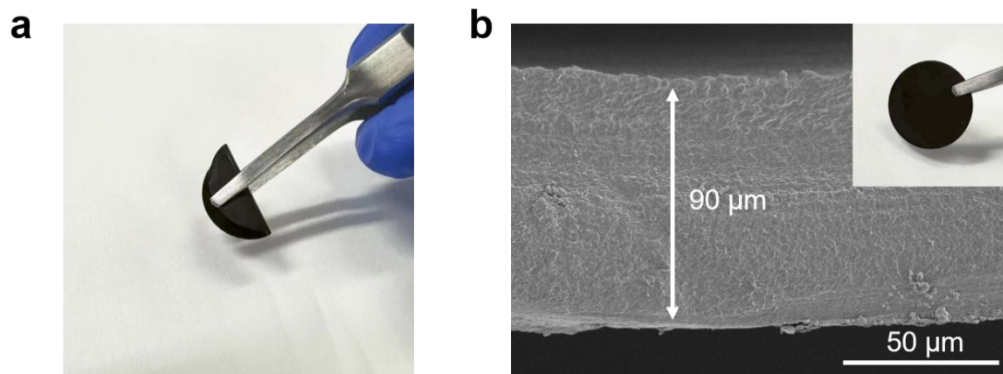
Fig. S6. TEM image of single h-PAN@MOF fiber.

Fig. S7. (a) Optical photograph and (b) cross-sectional SEM image of PPM electrolyte.
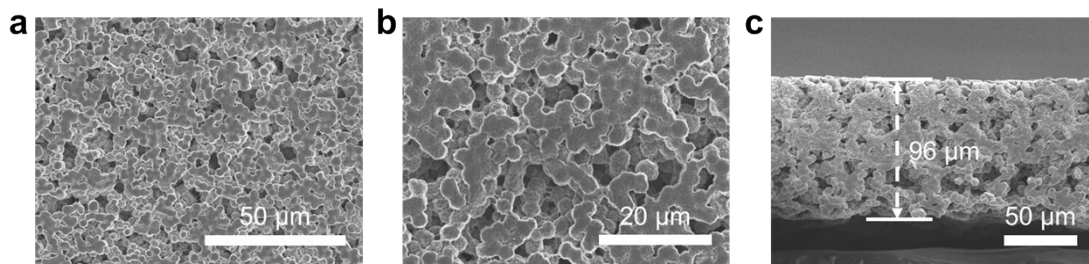
Fig. S8. (a, b) Surface and (c) cross-sectional SEM images of PVDF electrolyte.
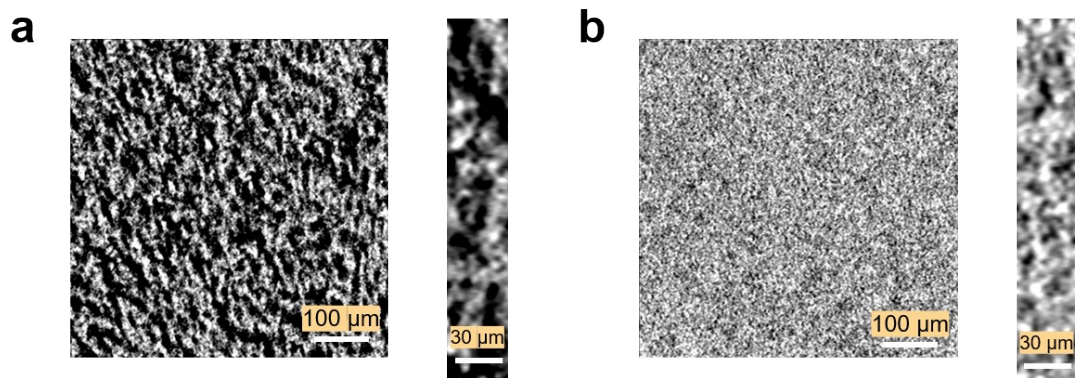
Fig. S9. Computed tomography (CT) images of (a) PVDF and (b) PPM electrolytes.
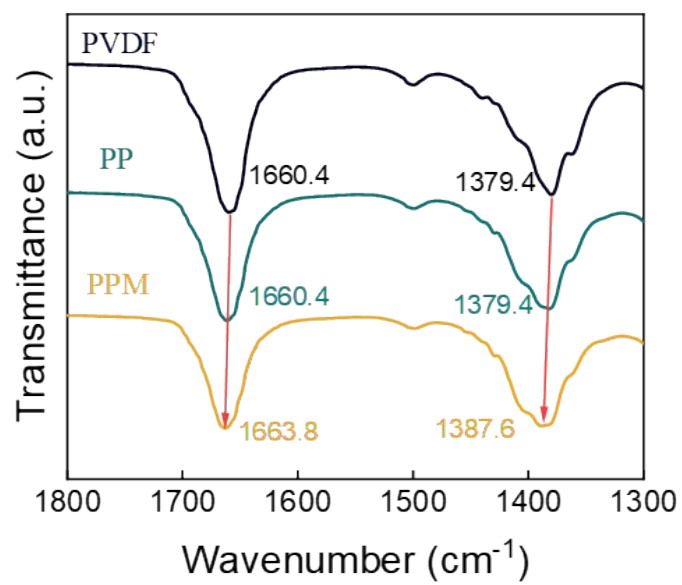
Fig. S10. FTIR spectra of the PVDF, PP and PPM electrolytes.
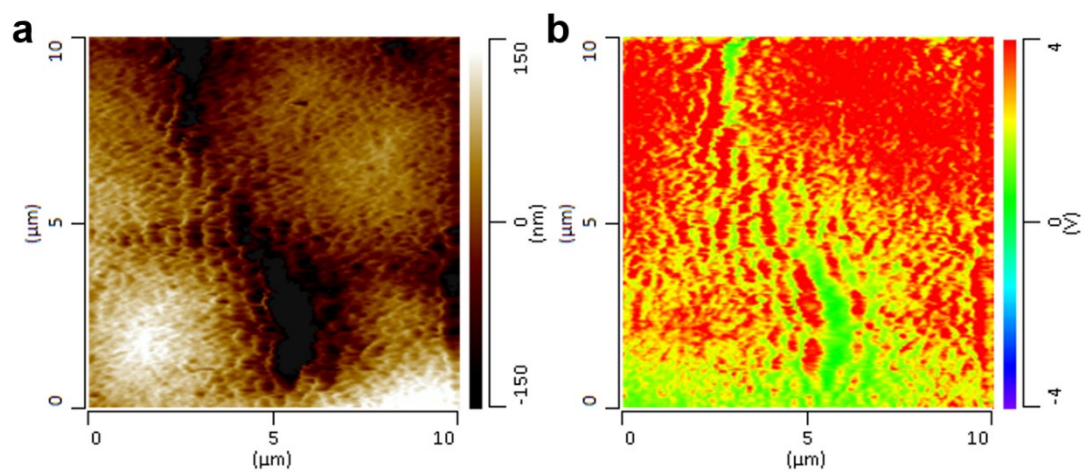
Fig. S11. (a) AFM image and (b) nano-IR overlap of C=O vibration of DMF at 1664 cm^{-1} of PVDF electrolyte.
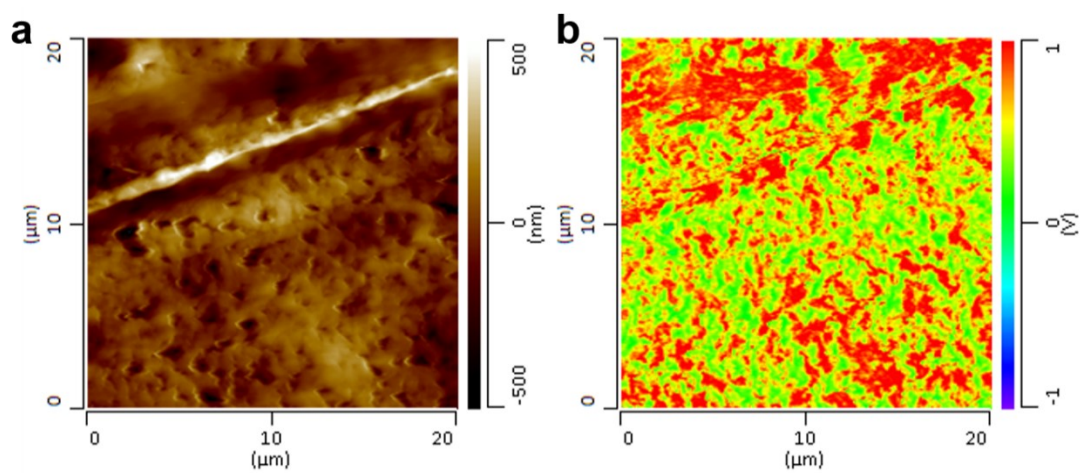
Fig. S12. (a) AFM image and (b) nano-IR overlap of C=O vibration of DMF at 1664 cm^{-1} of PP electrolyte.
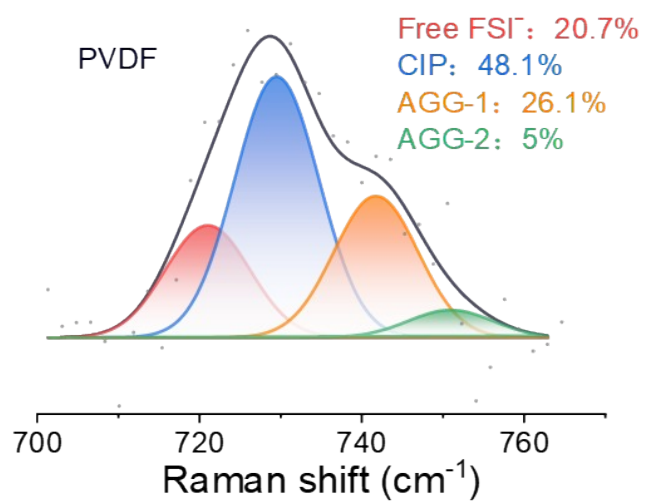
Fig. S13. Raman spectra of the S-N-S peak of FSI⁻ in PVDF electrolyte.
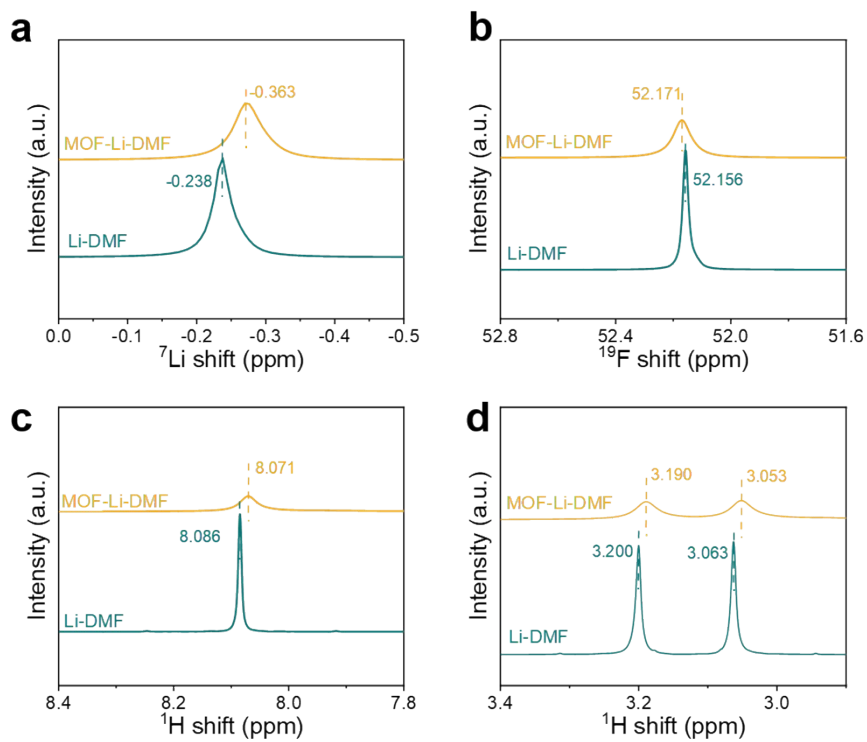
Fig. S14. Liquid NMR spectra of 8 M Li-DMF solutions and MOF-Li-DMF suspensions: (a) ^{7}Li, (b) ^{19}F and (c, d) ^{1}H spectra.
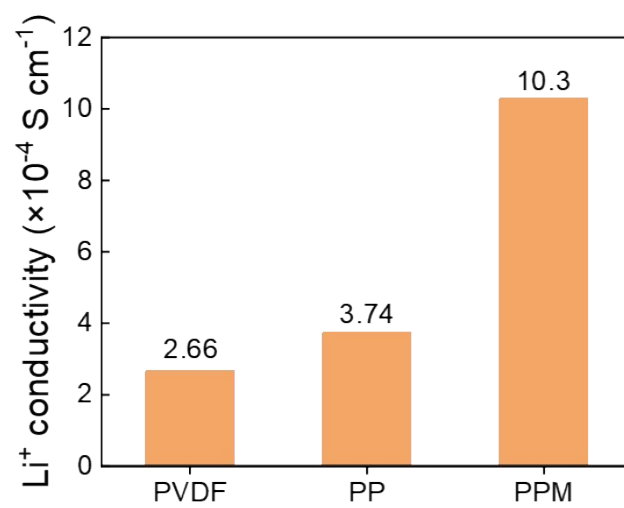
Fig. S15. Room-temperature ionic conductivities of PVDF, PP and PPM electrolytes.
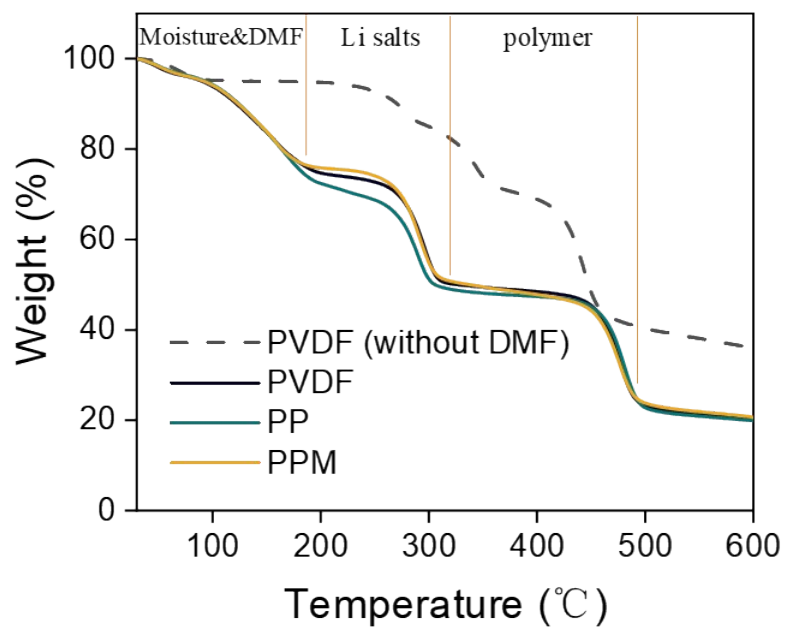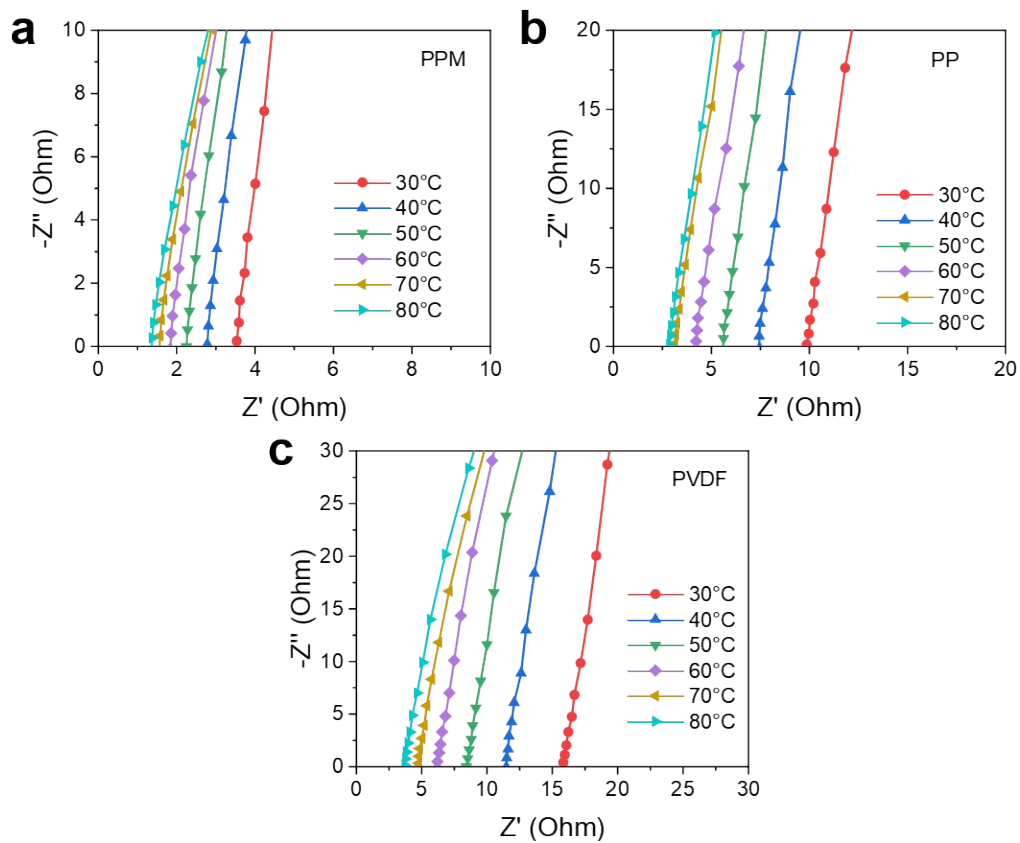
Fig. S16. TGA curves of the electrolytes.

Fig. S17. Ion transport activation energy tests of electrolytes. EIS of SS‖SS cells at different temperatures of (a) PPM, (b) PP and (c) PVDF electrolytes.
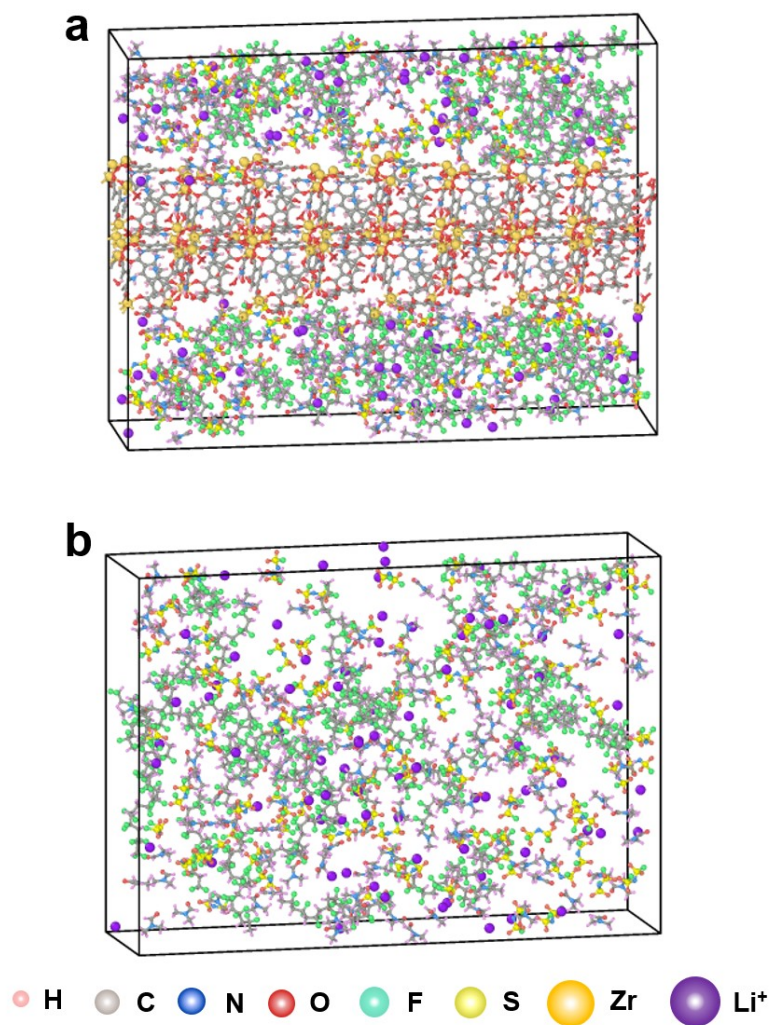
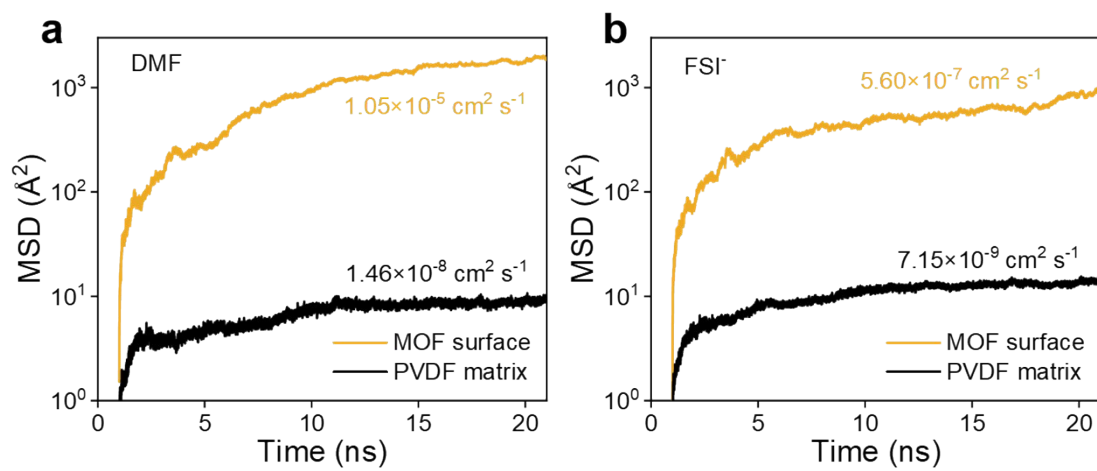**Fig. S18.** Structure geometries of the diffusion coefficient for (a) PPM and (b) PVDF electrolytes.

Fig. S19. Calculated mean square displacement (MSD) of (a) DMF and (b) FSI⁻ as a function of the simulation time.
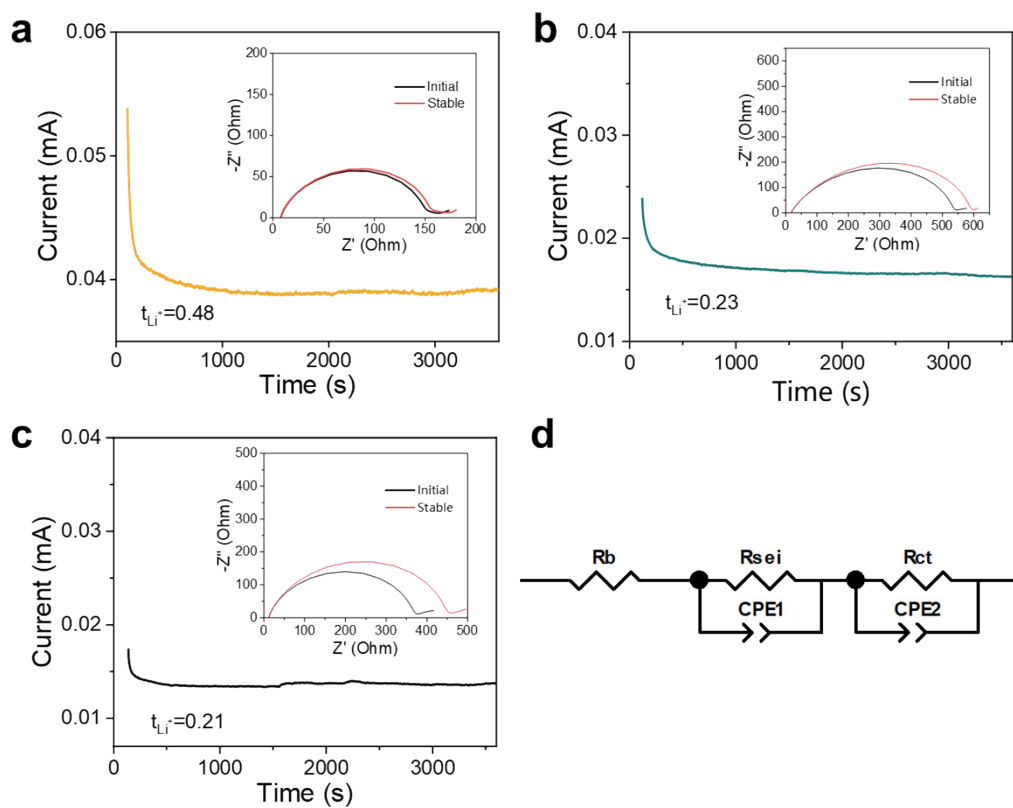
Fig. S20. Polarization curves as well as the initial and steady state EIS of (a) Li|PPM|Li, (b) Li|PP|Li and (c) Li|PVDF|Li cells. (d) Equivalent circuit of EIS.
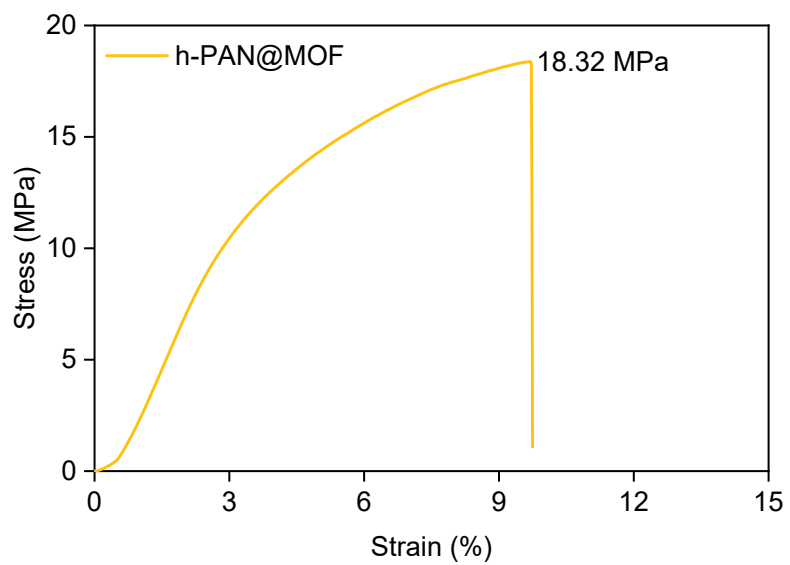
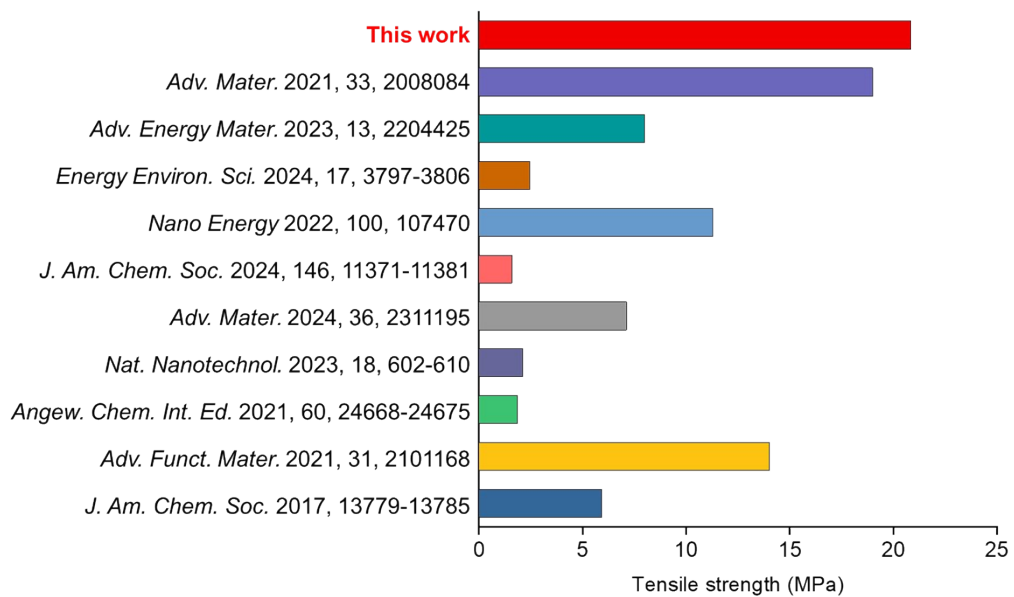**Fig. S21.** Stress-strain curves of h-PAN@MOF networks.

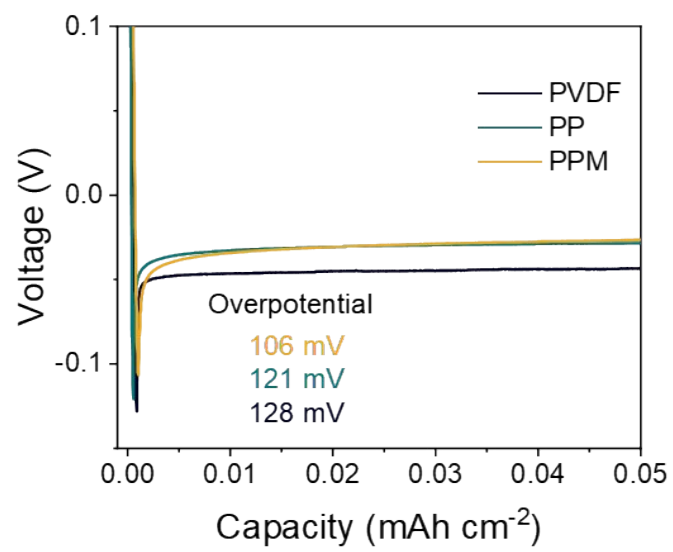**Fig. S22.** Comparison of tensile strength of PVDF-based composite solid electrolytes.

Fig. S23. Overpotential of Li|PVDF|Cu, Li|PP|Cu and Li|PPM|Cu cells.
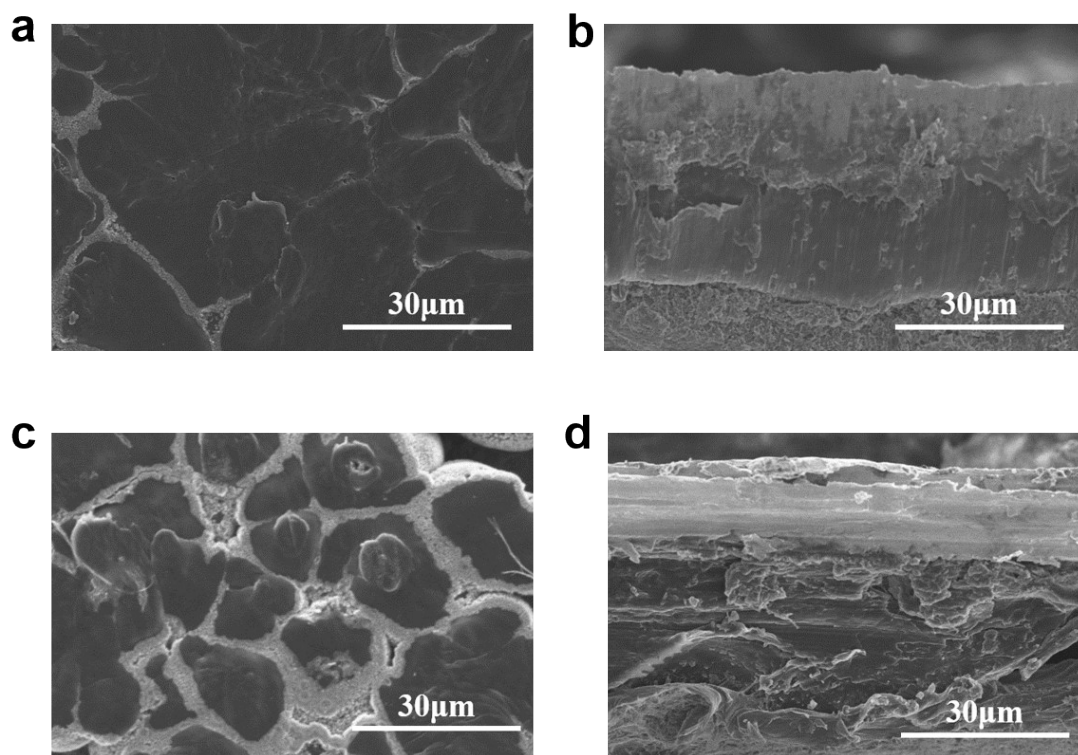
Fig. S24. SEM images of Li deposition in (a, b) Li|PPM|Cu and (c, d) Li|PVDF|Cu cells.

Fig. S25. Galvanostatic cycling profiles of the Li|PPM|Li, Li|PP|Li and Li|PVDF|Li cells for (a) 395-430 hours and (b) 1110-1145 hours at 0.1 mA cm^{-2}, 0.1 mAh cm^{-2}.

Fig. S26. Galvanostatic cycling profiles of the Li|PPM|Li, Li|PP|Li and Li|PVDF|Li cells for (a) 60-80 hours and (b) 450-480 hours at 0.5 mA cm^{-2}, 0.5 mAh cm^{-2}.
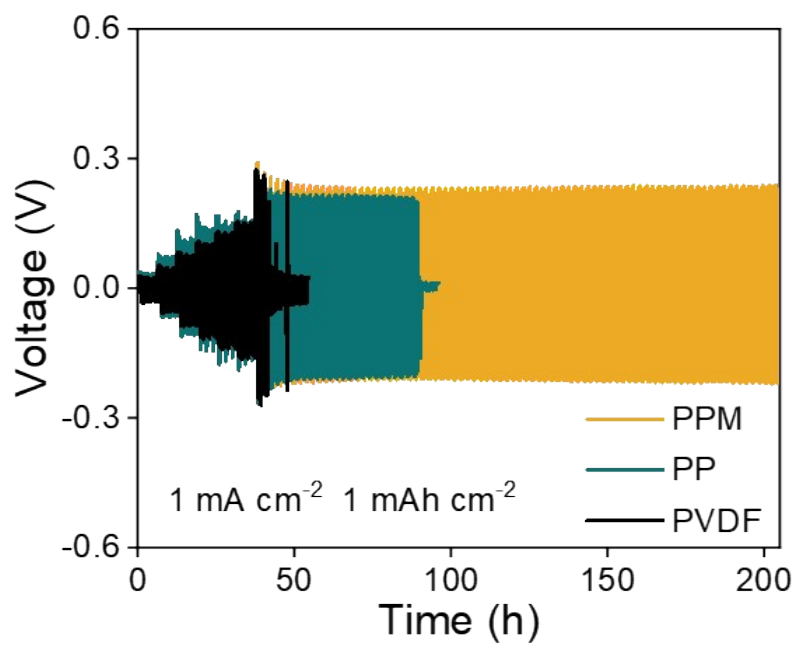
Fig. S27. Galvanostatic cycling curves of Li‖Li symmetric cells with PVDF, PP and PPM electrolytes at current densities of 1 mA cm^{-2}.
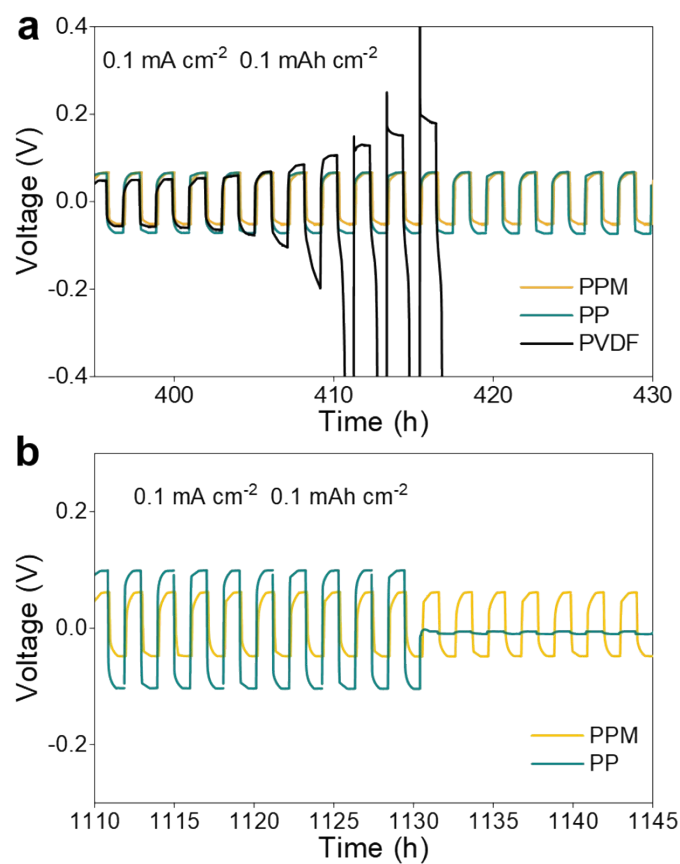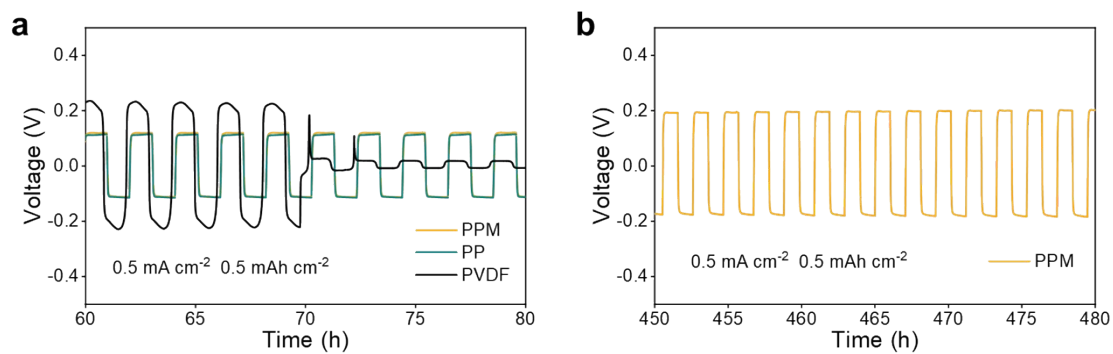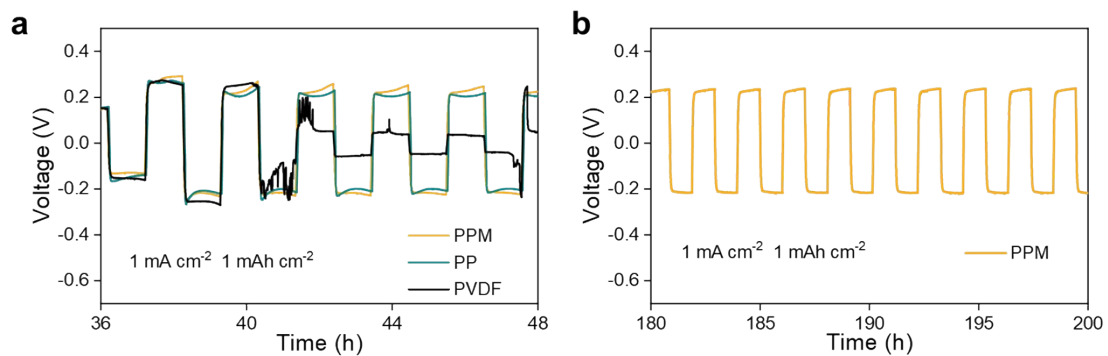
Fig. S28. Galvanostatic cycling profiles of the Li|PPM|Li, Li|PP|Li and Li|PVDF|Li cells for (a) 36-48 hours and (b) 180-200 hours at 1 mA cm^{-2}, 1 mAh cm^{-2}.
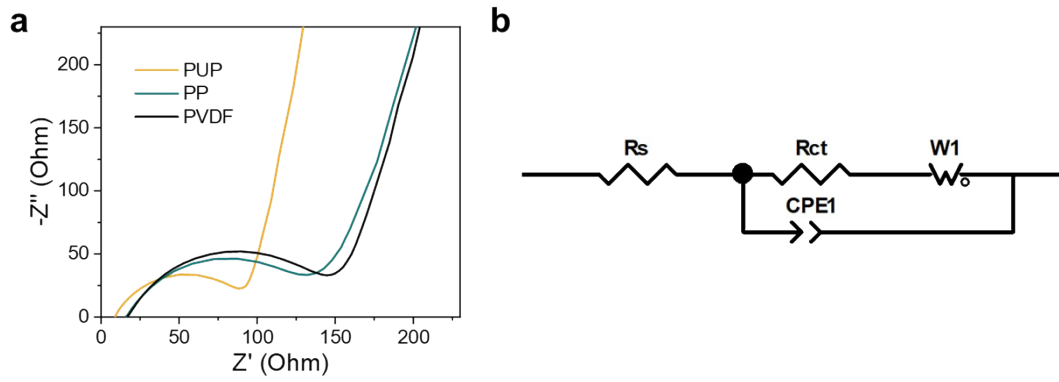
Fig. S29. (a) EIS of the Li|PVDF|NCM811, Li|PP|NCM811 and Li|PPM|NCM811 cells. (b) Equivalent circuit of EIS.
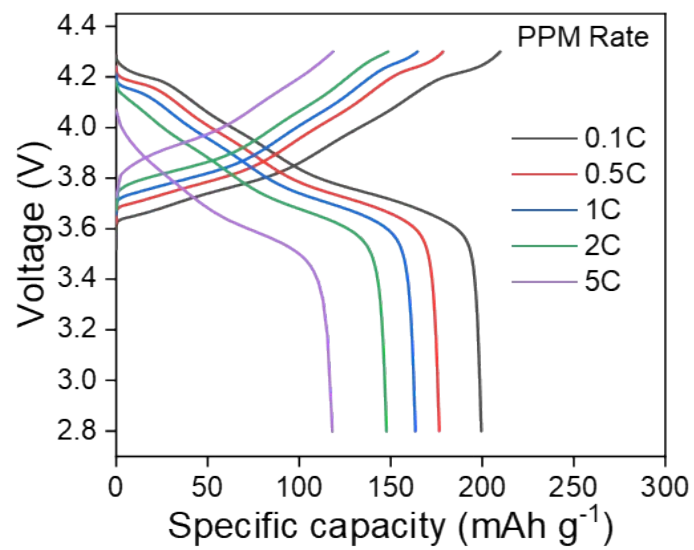
Fig. S30. Charge/discharge curves of Li|PPM|NCM811 cells at different rates.
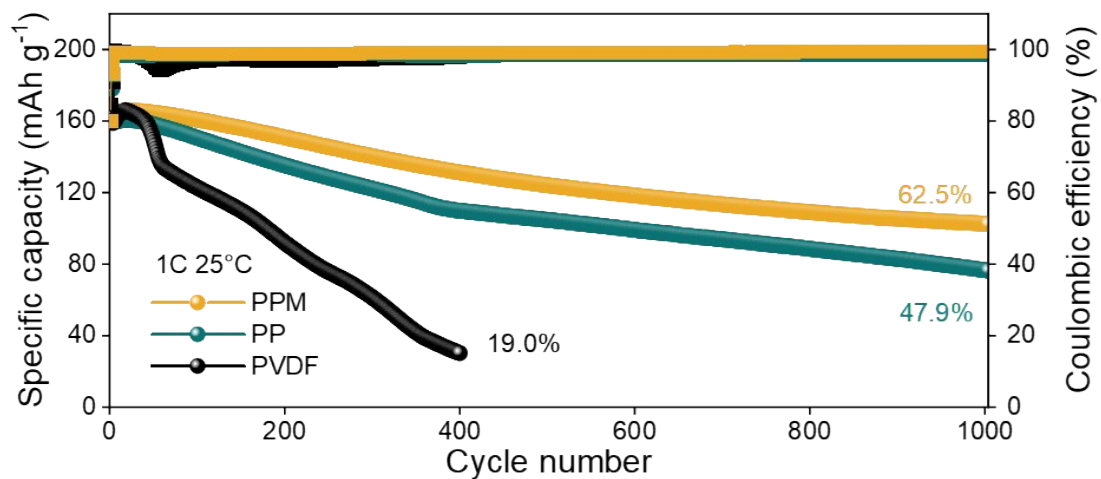
Fig. S31. Long-term cycling performance of Li|PVDF|NCM811, Li|PP|NCM811 and Li|PPM|NCM811 cells at 1C, 25 °C, 2.8-4.3 V.
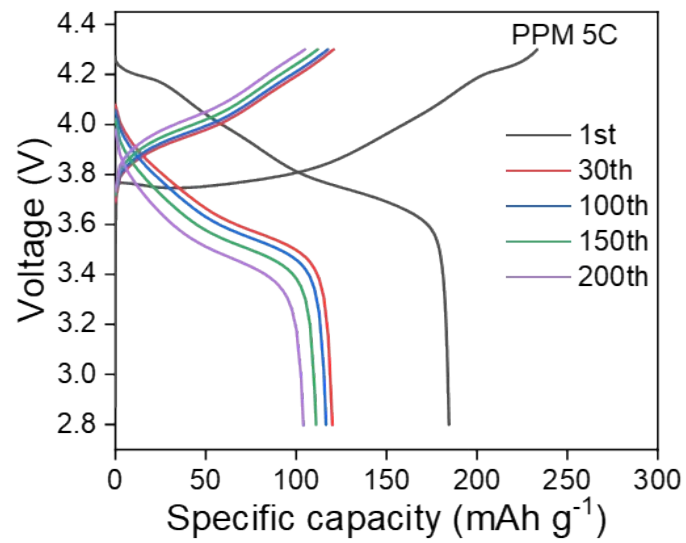
Fig. S32. Charge/discharge curves of Li|PPM|NCM811 cells at 5C.
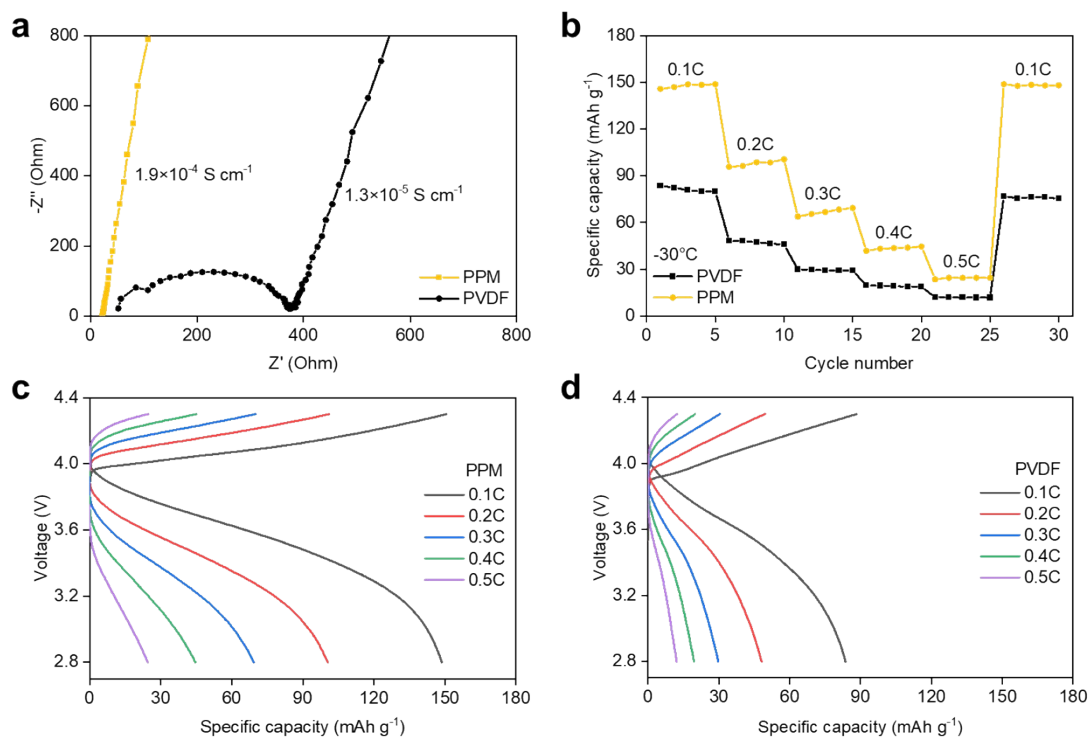
Fig. S33. (a) EIS of SS‖SS cells with PPM and PVDF electrolytes at -30°C. (b) Rate capacities of Li‖NCM811 cells at -30°C and charge/discharge curves with (c) PPM and (d) PVDF electrolytes.
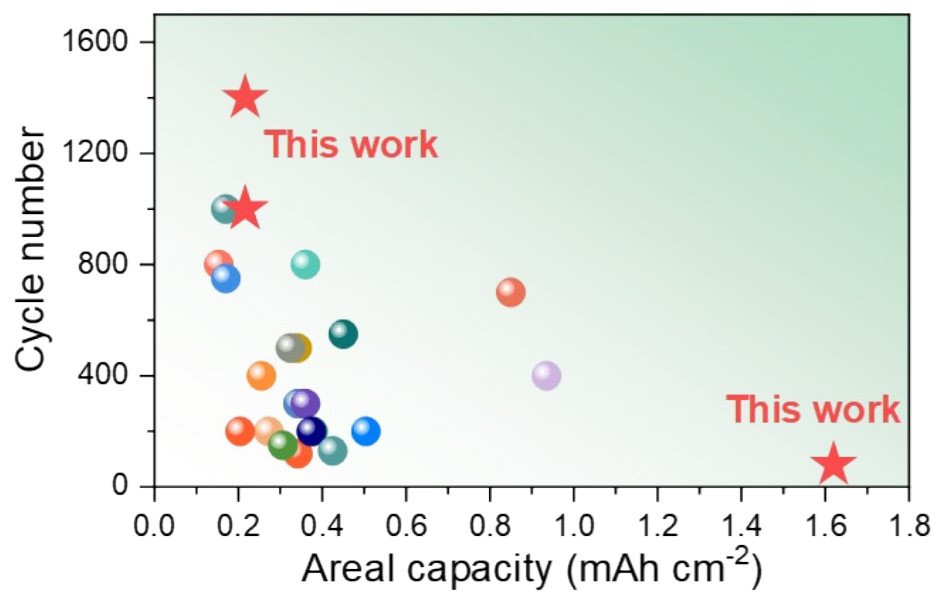
Fig. S34. Comparison of solid-state full batteries' performance. The related references are given in Table S1.
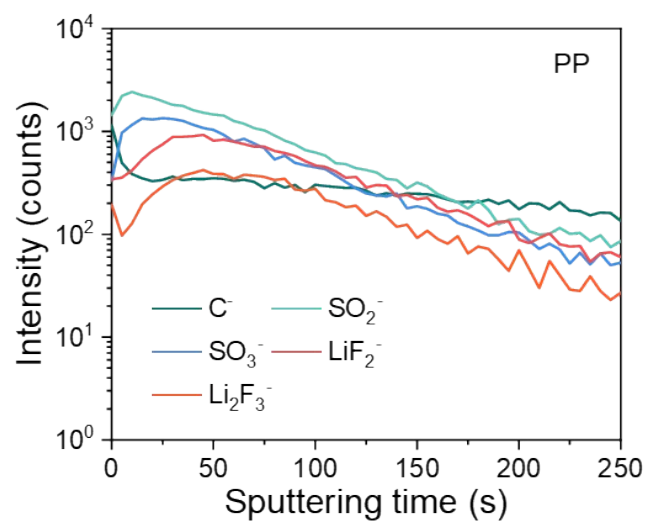
Fig. S35. TOF-SIMS depth profiling of several secondary ion fragments on the SEI using PP electrolyte.

Li$^+$ | Li$_2$OH$^-$ | SO$_2^-$ | Li$_2$F$_3^-$

SO$_3^-$ | CN$^-$ | C$_2$HO$^-$
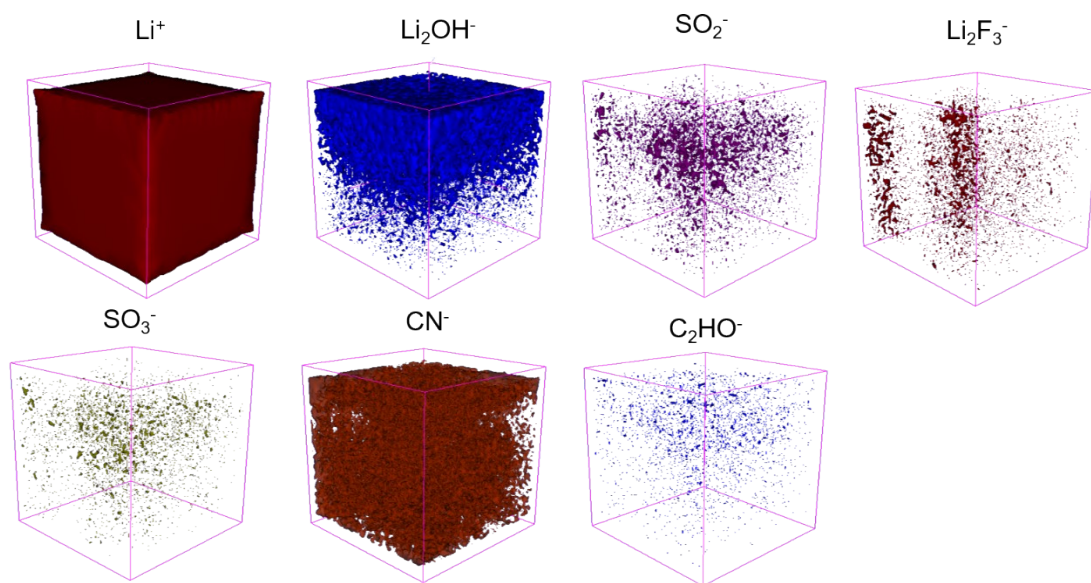
Fig. S36. TOF-SIMS 3D reconstruction of the sputtered volume on the SEI using PVDF electrolyte.
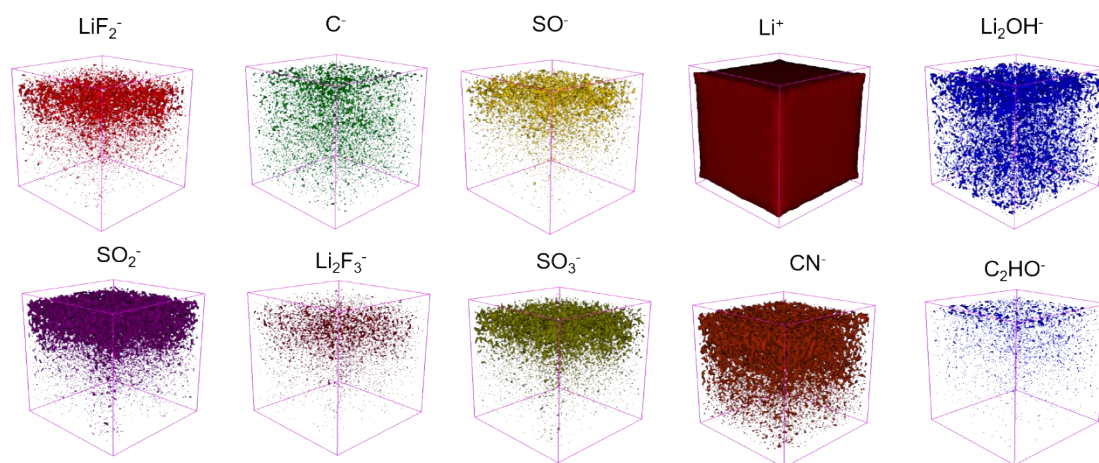
Fig. S37. TOF-SIMS 3D reconstruction of the sputtered volume on the SEI using PP electrolyte.
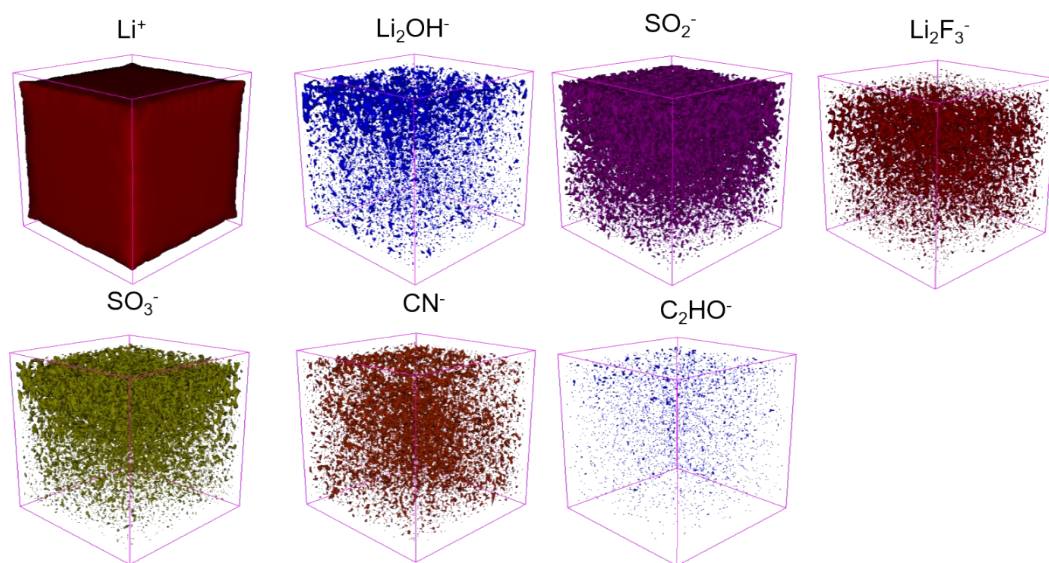
Fig. S38. TOF-SIMS 3D reconstruction of the sputtered volume on the SEI using PPM electrolyte.
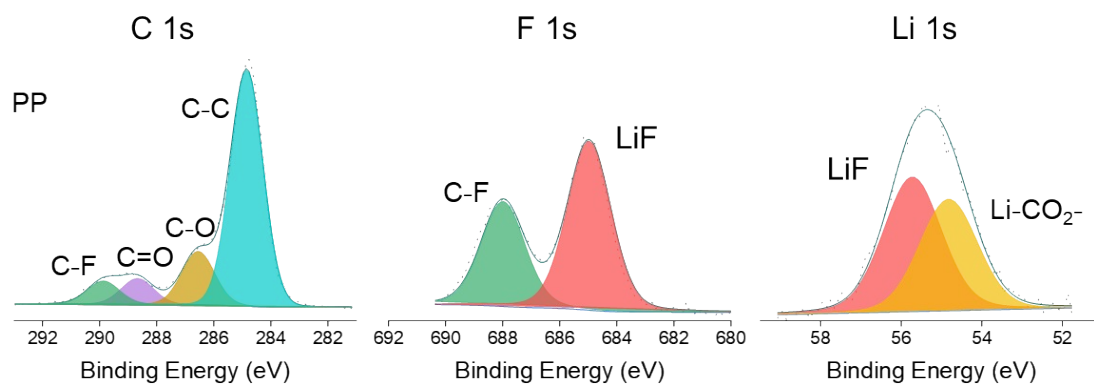
Fig. S39. XPS spectra of the SEI formed by PP electrolyte.
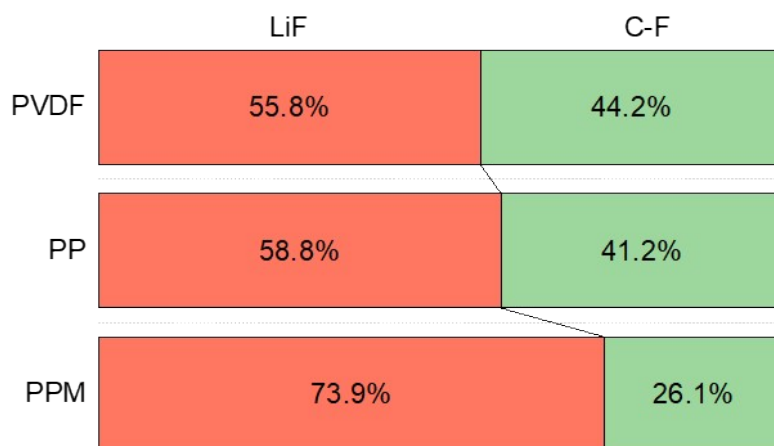
Fig. S40. Graph of the peak area ratio of XPS F 1*s* spectra with SEI in Li|PPM|Li, Li|PP|Li and Li|PVDF|Li cells.
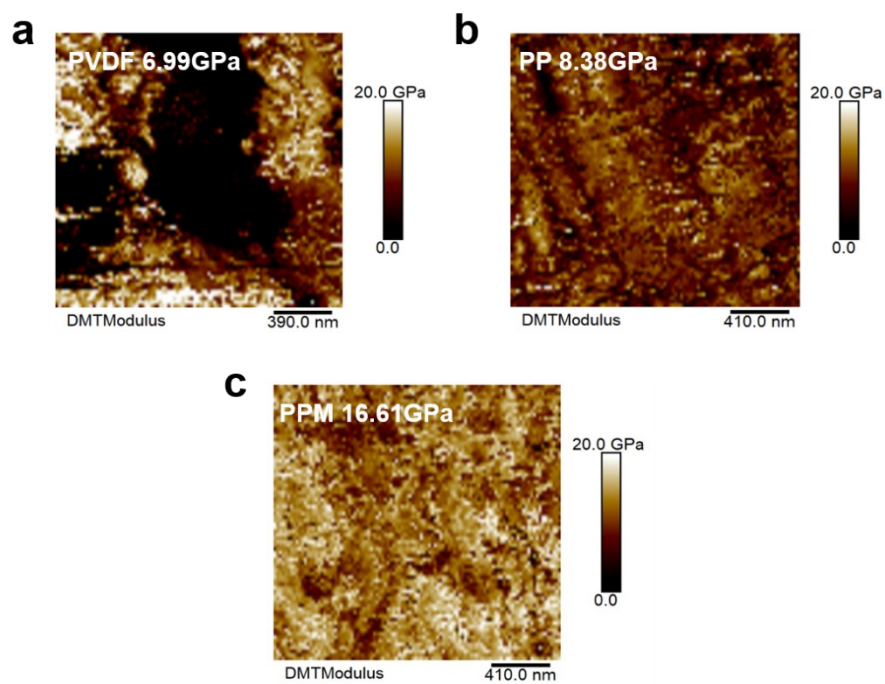
Fig. S41. AFM images of the SEI for Young's modulus tests using (a) PVDF, (b) PP and (c) PPM electrolytes.
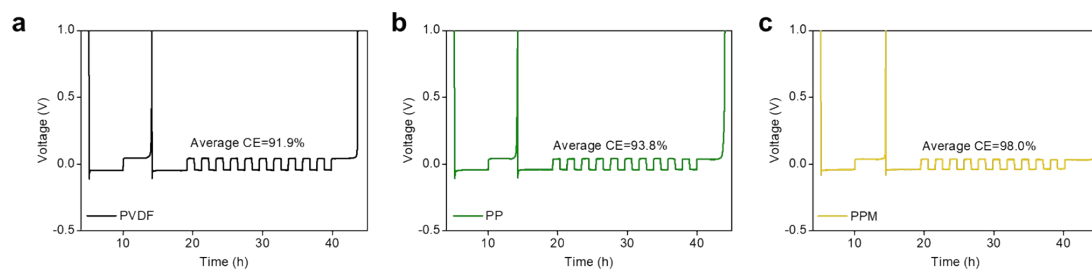
Fig. S42. Voltage profiles of Li‖Cu cells with (a) PVDF, (b) PP and (c) PPM electrolytes for the CE tests.
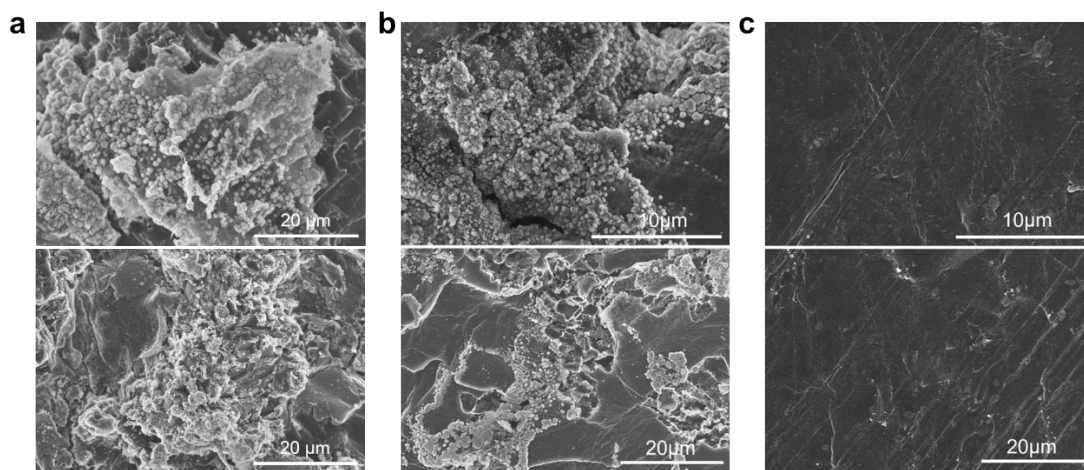
Fig. S43. Different magnification SEM images of the cycled Li metal with (a) PVDF, (b) PP and (c) PPM electrolytes after 200 h cycling.
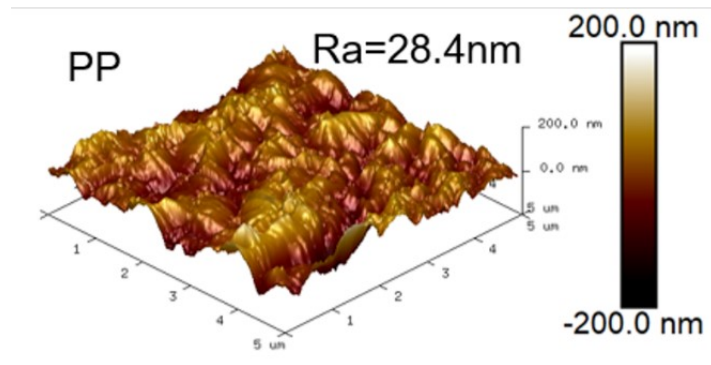
Fig. S44. AFM topography of cycled Li metal in Li∥Li symmetric cells with PP electrolyte.
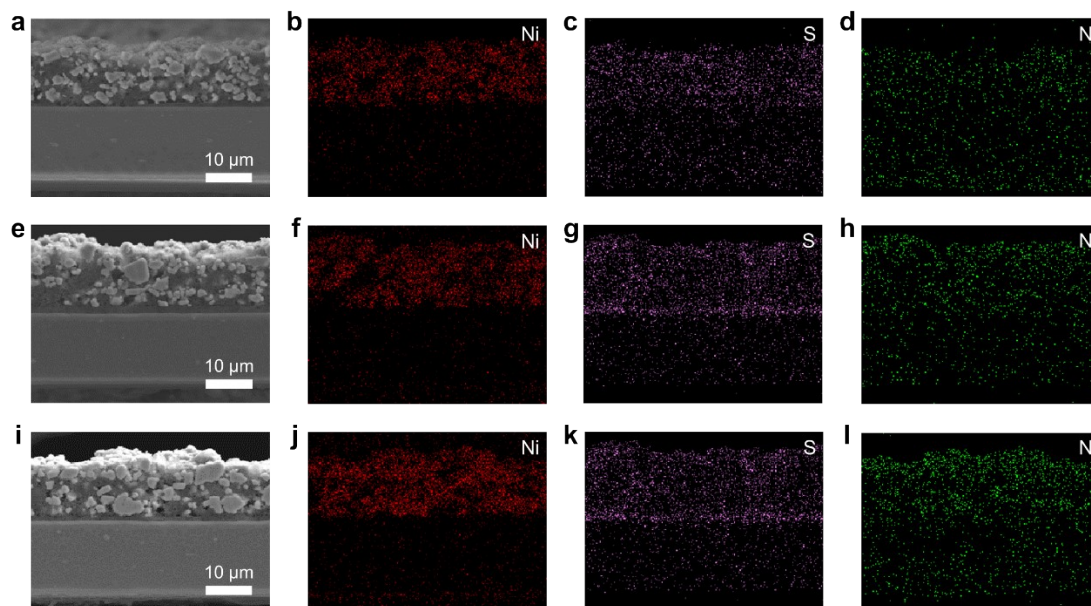
Fig. S45. (a) Cross-sectional SEM image of pristine NCM811 cathode contacted with PVDF electrolyte and EDS mappings of (b) Ni, (c) S and (d) N elements. (e) Cross-sectional SEM image of pristine NCM811 cathode contacted with PP electrolyte and EDS mappings of (f) Ni, (g) S and (h) N elements. (i) Cross-sectional SEM image of pristine NCM811 cathode contacted with PVDF electrolyte and EDS mappings of (j) Ni, (k) S and (l) N elements.
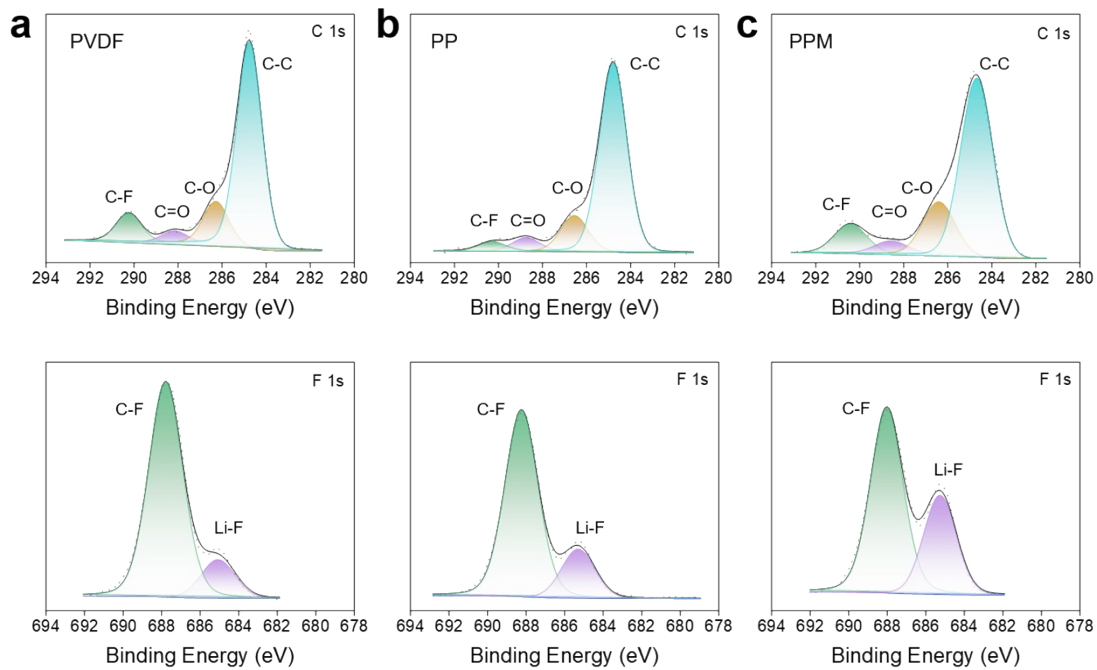
Fig. S46. XPS spectra of the CEI formed by (a) PVDF, (b) PP and (c) PPM electrolytes.
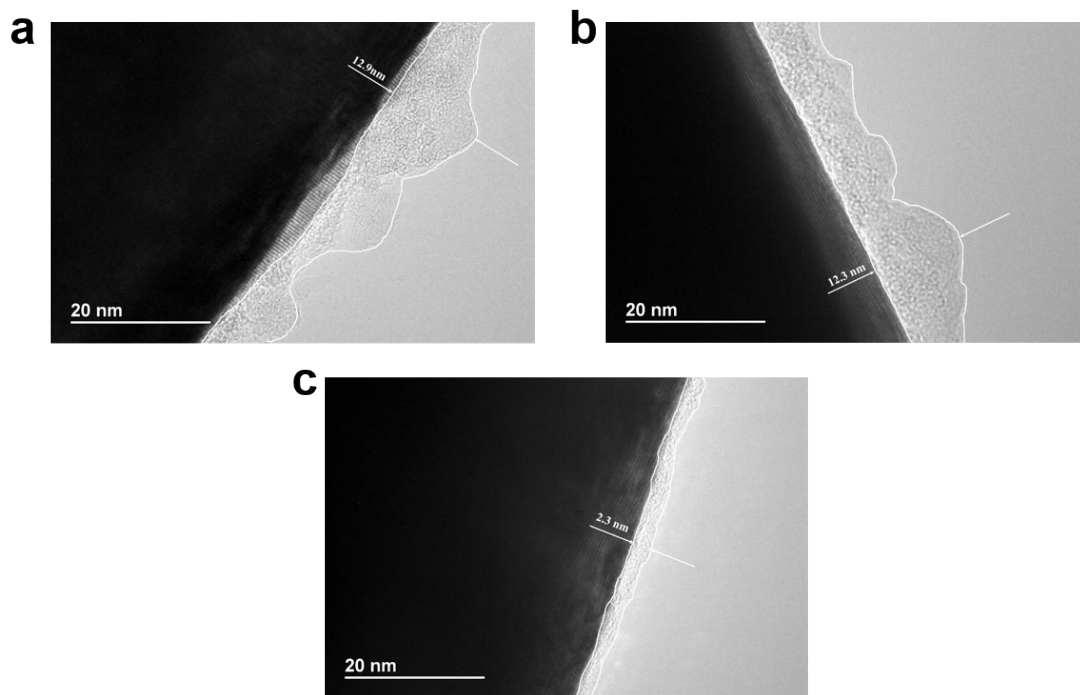
Fig. S47. TEM images of the CEI on cycled NCM811 with (a) PVDF, (b) PP and (c) PPM electrolytes.
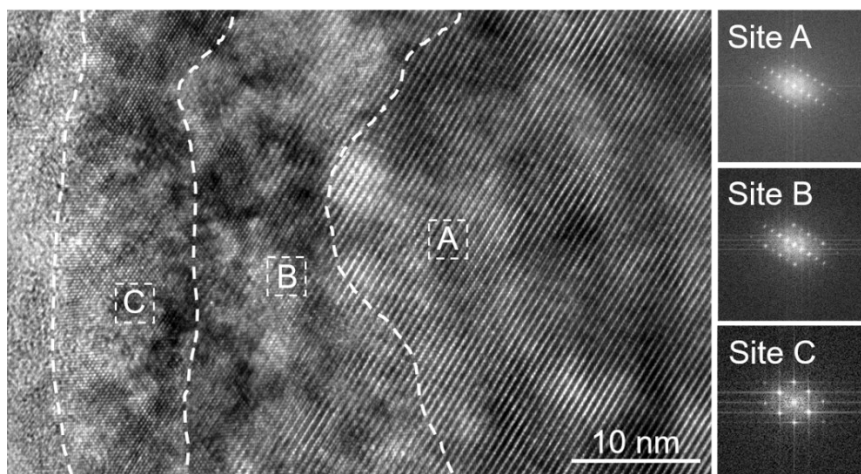
Fig. S48. TEM and FFT images of cycled NCM811 cathode with PP electrolyte.

Supplementary Tables

Table S1. Comparison of room-temperature ionic conductivity and critical current density of PVDF-based composite solid electrolytes.

Electrolytes	Room-temperature ionic conductivity ($S\ cm^{-1}$)	Critical current density ($mA\ cm^{-2}$)	References
PVDF-b-PTFE/LiTFSI/LLZAO/LLTO	1.38×10^{-4}	/	*Adv. Mater.* 2021, 33, 2008084[21]
PVDF/LiClO$_4$/LLZTO	5.0×10^{-4}	/	*J. Am. Chem. Soc.* 2017, 139, 13779-13785[22]
PVDF/LiFSI/LATP nanowires	6.0×10^{-4}	2.2	*Angew. Chem. Int. Ed.* 2021, 60, 24668-24675[23]
PVDF-HFP-LiTFSI/LLZNO nanowires/MOFs particles	2.0×10^{-4}	/	*Adv. Energy Mater.* 2020, 10, 2000709[24]
PVDF/LiFSI/zeolite molecular sieves	4.5×10^{-4}	1.3	*Angew. Chem. Int. Ed.* 2024, 63, e202401428[25]
PVDF/LiFSI/BTO-LLTO nanowires	8.2×10^{-4}	2.5	*Nat. Nanotechnol.* 2023, 18, 602-610[26]
PVDF/LiFSI/5wt% Li$_{0.025}$Na$_{0.975}$NbO$_3$	5.56×10^{-4}	2.58	*Adv. Mater.* 2024, 36, 2311195[27]
PVDF/LiFSI/DMF and TFA/LATP nanowires	7.0×10^{-4}	2.9	*J. Am. Chem. Soc.* 2024, 146, 16, 11371-11381[28]
PVDF/LiFSI/g-C$_3$N$_4$	6.9×10^{-4}	2	*Nano Energy* 2022, 100, 107470[29]
PVDF/LiFSI/MoSe$_2$	6.5×10^{-4}	2.3	*Nat. Commun.* 2023, 14, 6296[30]
PVDF/LiFSI/tetragonal-BaTiO$_3$	8.4×10^{-4}	2.2	*Energy Environ. Sci.* 2024, 17, 3797-3806[31]
PVDF-b-PTFE/LiTFSI/CuPcLi	8×10^{-4}	1.9	*Adv. Energy Mater.* 2023, 13, 2204425[32]
PPM	$\mathbf{1.03 \times 10^{-3}}$	**2.8**	**This work**

Table S2. Comparison of Li‖Li symmetric batteries' performance.

Solid-state electrolyte	Performance	References
PVDF/LiClO$_4$/LLZTO	0.05 mA cm^{-2}-0.025 mAh cm^{-2} for 160 h	*J. Am. Chem. Soc.* 2017, 139, 13779-13785[22]
PVDF/LiTFSI-LiDFOB-LiBF$_4$	0.25 mA cm^{-2}-0.25 mAh cm^{-2} for 270 h	*J. Am. Chem. Soc.* 2023, 145, 47, 25632-25642[33]
PVDF-*b*-PTFE/LiTFSI/LLZAO/LLTO	0.2 mA cm^{-2}-0.2 mAh cm^{-2} for 1880 h	*Adv. Mater.* 2021, 33, e2008084[21]
PVDF-HFP/LiTFSI	0.3 mA cm^{-2}-0.15 mAh cm^{-2} for 300 h	*Angew. Chem. Int. Ed.* 2021, 60, 12931-12940[34]
P(VDF-TrFE-CTFE)/LiTFSI	0.05 mA cm^{-2}-0.05 mAh cm^{-2} for 1200 h	*Energy Environ. Sci.* 2021, 14, 6021-6029[35]
PVDF/LiFSI/LATP nanowires	0.1 mA cm^{-2}-0.1 mAh cm^{-2} for 2600 h	*Angew. Chem. Int. Ed.* 2021, 60, 24668-24675[23]
PVDF/LiTFSI/DMIm	0.1 mA cm^{-2}-0.05 mAh cm^{-2} for 800 h	*Angew. Chem. Int. Ed.* 2022, 61, e202205075[36]
PVDF/LiTFSI/LLZTO@PDA	0.1 mA cm^{-2}-0.1 mAh cm^{-2} for 1000 h	*Adv. Energy Mater.* 2023, 13, 2204377[37]
PVDF-HFP-LiTFSI/LLZNO nanowires/MOFs particles	0.25 mA cm^{-2}-0.125 mAh cm^{-2} for 1700 h	*Adv. Energy Mater.* 2020, 10, 2000709[24]
P(VDF-TrFE-CTFE)/(Pyr13-TFSI)	0.1 mA cm^{-2}-0.05 mAh cm^{-2} for 1500 h	*Angew. Chem. Int. Ed.* 2023, 62, e202300243[38]
PVDF/LiFSI/zeolite molecular sieves	0.5 mA cm^{-2}-0.5 mAh cm^{-2} for 200 h	*Angew. Chem. Int. Ed.* 2024, 63, e202401428[25]
PVDF-HFP/LiTFSI/SiO$_2$	0.2 mA cm^{-2}-0.2 mAh cm^{-2} for 3000 h	*Adv. Mater.* 2022, 34, e2205575[39]
PVDF-HFP/LiTFSI/Fluorinated graphene	0.5 mA cm^{-2}-0.5 mAh cm^{-2} for 360 h	*Adv. Energy Mater.* 2022, 12, 2200967[40]
PVDF/Li$_4$Ti$_5$O$_{12}$	0.3 mA cm^{-2}-0.5 mAh cm^{-2} for 600 h	*Adv. Energy Mater.* 2022, 12, 2201991[41]
VEC/MASTFSILi/SN	0.1 mA cm^{-2}-0.1 mAh cm^{-2} for 1000 h	*Adv. Mater.* 2022, 34, e2202143[42]
PVDF/LiFSI/5wt% Li$_{0.025}$Na$_{0.975}$NbO$_3$	0.1 mA cm^{-2}-0.1 mAh cm^{-2} for 2800 h	*Adv. Mater.* 2023, 36, 2311195[27]
C$_3$mpyrFSI/LiFSI	0.2 mA cm^{-2}-0.2 mAh cm^{-2} for 2000 h	*Nat. Mater.* 2021, 20, 1255-1263[43]

COF/LiTFSI/DMA	0.3 mA cm^{-2}-0.075 mAh cm^{-2} for 450 h	*Adv. Mater.* 2022, 34, e2201410[44]
PEGDA/UpyMA/LiTFSI/ NML	0.2 mA cm^{-2}-0.2 mAh cm^{-2} for 2250 h	*Energy Environ. Sci.* 2022, 15, 5149-5158[45]
(Adpn)$_2$LiPF$_6$	0.01 mA cm^{-2}-0.02 mAh cm^{-2} for 600 h	*Nat. Mater.* 2023, 22, 627-635[46]
IL/VEC/OFHDODA /LiTFSI	0.1 mA cm^{-2}-0.1 mAh cm^{-2} for 2500 h	*Nat. Commun.* 2023, 14, 2301[47]
PPM	**0.1 mA cm^{-2}-0.1 mAh cm^{-2} for 3200 h**	**This work**
PPM	**0.5 mA cm^{-2}-0.5 mAh cm^{-2} for 500 h**	**This work**
PPM	**1mA cm^{-2}-1 mAh cm^{-2} for 160 h**	**This work**

Table S3. Comparison of solid-state full batteries' performance.

Solid-state electrolyte	Areal capacity (mAh cm^{-2})	Current density (mA cm^{-2})	Cut-off voltage (V)	Cathode material	Cycle number	References
PVDF/LiClO$_4$/ LLZTO	0.342	0.1	4.2	LCO	120	*J. Am. Chem. Soc.* 2017, 139, 13779-13785[22]
PVDF/LiFSI	0.504	0.15	4.2	LCO	200	*Adv. Mater.* 2019, 31, 1806082[48]
PVDF-*b*-PTFE/LiTFSI/ LLZAO/LLTO	0.45	0.225	4.35	NCM532	550	*Adv. Mater.* 2021, 33, e2008084[21]
PVDF-HFP/LiTFSI	0.378	0.075	4.3	NCM532	200	*Angew. Chem. Int. Ed.* 2021, 60, 12931-12940[34]
P(VDF-TrFE-CTFE)/LiTFSI	0.272	0.136	4.2	LFP	200	*Energy Environ. Sci.* 2021, 14, 6021-6029[35]
PVDF/LiTFSI/ DMIm	0.153	0.306	4	LFP	800	*Angew. Chem. Int. Ed.* 2022, 61, e202205075[36]
PVDF-HFP/LiTFSI/SiO$_2$	0.935	0.187	4	LFP	400	*Adv. Mater.* 2022, 34, e2205575[39]
PVDF-HFP/LiTFSI	0.36	0.36	4.2	NCM811	800	*Energy Environ. Sci.* 2022, 15, 3379-3387[45]
PVDF/LiFSI/BTO/LLTO	0.288	0.288	4.3	NCM811	1500	*Nat. Nanotechnol.* 2023, 18, 602-610[26]
P(VDF-TrFE-CTFE)/(Pyr13-TFSI)	0.17	0.17	4.2	LFP	1000	*Angew. Chem. Int. Ed.* 2023, 62, e202300243[38]
PVDF-HFP/LiTFSI/Fluorinated graphene	0.342	0.342	4.2	NCM622	300	*Adv. Energy Mater.* 2022, 12, 2200967[40]
PVDF/LiFSI/Zeolite	0.252~0.324	0.504~0.648	4.3	NCM811	500	*Angew. Chem. Int. Ed.* 2024, e202401428[25]
PVDF/LiFSI/ MOF network	0.34	0.17	4	LFP	500	*Adv. Energy Mater.* 2022, 12, 2200501[49]
PVDF/LiTFSI-LiDFOB-LiBF$_4$	0.18~0.36	0.09~0.18	4.2	NCM811	300	*J. Am. Chem.Soc.* 2023, 145, 25632–25642[33]

PVDF/LiTFSI/ LLZTO@PDA	0.374	0.0374	4	LFP	200	*Adv. Energy Mater.* 2023, 13, 2204377[37]
PVDF-HFP/LiTFSI/L LZNO nanowires/MO Fs particles	0.306	0.306	4.2	LCO180	150	*Adv. Energy Mater.* 2020, 2000709[24]
MOF with customized bilayer zwitterionic nanochannels/ LiTFSI	0.204	0.102	4	LFP	200	*Adv. Mater.* 2023, 35, 2304685[50]
VEC/MASTFS ILi/SN	0.255	0.255	4	LFP	400	*Adv. Mater.* 2022, 34, e220214349[42]
Al(Otf)$_3$-LiTFSI/DOL	0.85	0.85	4	LFP	700	*Nat. Energy* 2019, 4, 365-373[51]
COF/LiTFSI/D MA	0.425	0.1	3.8	LFP	130	*Adv. Mater.* 2022, 34, e2201410[44]
COF/LiClO$_4$	0.17	0.17	4.2	LFP	750	*Nat. Commun.* 2022, 13, 2031[52]
PPM	**0.216**	**1.08**	**4.3**	**NCM811**	**1000**	**This work**
PPM	**1.62**	**0.162**	**4.3**	**NCM811**	**80**	**This work**
PPM	**0.81**	**0.405**	**4.3**	**NCM811**	**190**	**This work**
PPM	**0.216**	**0.216**	**4.3**	**NCM811**	**1000**	**This work**
PPM	**0.216**	**0.432**	**4.3**	**NCM811**	**1400**	**This work**

Supplementary References

1. J. Zhao, D. T. Lee, R. W. Yaga, M. G. Hall, H. F. Barton, I. R. Woodward, C. J. Oldham, H. J. Walls, G. W. Peterson and G. N. Parsons, *Angew. Chem. Int. Ed.*, 2016, **55**, 13224-13228.

2. B. D. Adams, J. Zheng, X. Ren, W. Xu and J. G. Zhang, *Adv. Energy Mater.*, 2017, **8**, 1702097.

3. G. Kresse and J. Furthmüller, *Phys. Rev. B*, 1996, **54**, 11169-11186.

4. S. Grimme, S. Ehrlich and L. Goerigk, *J. Comput. Chem.*, 2011, **32**, 1456-1465.

5. P. E. Blochl, *Phys. Rev. B. Condens. Matter.*, 1994, **50**, 17953-17979.

6. S. Grimme, J. Antony, S. Ehrlich and H. Krieg, *J. Chem. Phys.*, 2010, **132**, 154104-154104-154119.

7. V. Wang, N. Xu, J.-C. Liu, G. Tang and W.-T. Geng, *Computer Physics Communications*, 2021, **267**, 108033.

8. S. Plimpton, *J. Comput. Phys.*, 1995, **117**, 1-19.

9. A. K. Rappe, C. J. Casewit, K. S. Colwell, W. A. Goddard and W. M. Skiff, *J. Am. Chem. Soc.*, 1992, **114**, 10024-10035.

10. W. L. Jorgensen, D. S. Maxwell and J. Tirado-Rives, *J. Am. Chem. Soc.*, 1996, **118**, 11225-11236.

11. G. A. Kaminski, R. A. Friesner, J. Tirado-Rives and W. L. Jorgensen, *J. Phys. Chem. B*, 2001, **105**, 6474-6487.

12. P. G. Boyd, S. M. Moosavi, M. Witman and B. Smit, *J. Phys. Chem. Lett.*, 2017, **8**, 357-363.

13. K. P. Jensen and W. L. Jorgensen, *J. Chem. Theory Comput.*, 2006, **2**, 1499-1509.

14. J. N. Canongia Lopes, K. Shimizu, A. A. H. Pádua, Y. Umebayashi, S. Fukuda, K. Fujii and S.-i. Ishiguro, *J. Phys. Chem. B*, 2008, **112**, 9449-9455.

15. N. N. Rajput, V. Murugesan, Y. Shin, K. S. Han, K. C. Lau, J. Chen, J. Liu, L. A. Curtiss, K. T. Mueller and K. A. Persson, *Chem. Mater.*, 2017, **29**, 3375-3379.

16. T. Lu and F. Chen, *J. Comput. Chem.*, 2012, **33**, 580-592.

17. D. E. Woon and T. H. Dunning, *J. Chem. Phys.*, 1993, **98**, 1358-1371.

18. C. Campañá, B. Mussard and T. K. Woo, *J. Chem. Theory Comput.*, 2009, **5**, 2866-2878.

19. L. Martínez, R. Andrade, E. G. Birgin and J. M. Martínez, *J. Comput. Chem.*, 2009, **30**, 2157-2164.

20. A. I. Jewett, D. Stelter, J. Lambert, S. M. Saladi, O. M. Roscioni, M. Ricci, L. Autin, M. Maritan, S. M. Bashusqeh, T. Keyes, R. T. Dame, J.-E. Shea, G. J. Jensen and D. S. Goodsell, *J. Mol. Biol.*, 2021, **433**, 166841-166841.

21. S. Liu, Y. Zhao, X. Li, J. Yu, J. Yan and B. Ding, *Adv. Mater.*, 2021, **33**, 2008084.

22. X. Zhang, T. Liu, S. Zhang, X. Huang, B. Xu, Y. Lin, B. Xu, L. Li, C.-W. Nan and Y. Shen, *J. Am. Chem. Soc.*, 2017, **139**, 13779-13785.

23. K. Yang, L. Chen, J. Ma, C. Lai, Y. Huang, J. Mi, J. Biao, D. Zhang, P. Shi, H. Xia, G. Zhong, F. Kang and Y.-B. He, *Angew. Chem. Int. Ed.*, 2021, **60**, 24668-24675.

24. J. Sun, X. Yao, Y. Li, Q. Zhang, C. Hou, Q. Shi and H. Wang, *Adv. Energy Mater.*, 2020, **10**, 2000709.

25. W. Yang, Y. Liu, X. Sun, Z. He, P. He and H. Zhou, *Angew. Chem. Int. Ed.*, 2024, **63**,

e202401428.

26. P. Shi, J. Ma, M. Liu, S. Guo, Y. Huang, S. Wang, L. Zhang, L. Chen, K. Yang, X. Liu, Y. Li, X. An, D. Zhang, X. Cheng, Q. Li, W. Lv, G. Zhong, Y.-B. He and F. Kang, *Nat. Nanotechnol.*, 2023, **18**, 602-610.

27. X. An, Y. Liu, K. Yang, J. Mi, J. Ma, D. Zhang, L. Chen, X. Liu, S. Guo, Y. Li, Y. Ma, M. Liu, Y.-B. He and F. Kang, *Adv. Mater.* 2024, **36**, 2311195.

28. K. Yang, J. Ma, Y. Li, J. Jiao, S. Jiao, X. An, G. Zhong, L. Chen, Y. Jiang, Y. Liu, D. Zhang, J. Mi, J. Biao, B. Li, X. Cheng, S. Guo, Y. Ma, W. Hu, S. Wu, J. Zheng, M. Liu, Y.-B. He and F. Kang, *J. Am. Chem. Soc.*, 2024, **146**, 11371-11381.

29. L. Chen, T. Gu, J. Ma, K. Yang, P. Shi, J. Biao, J. Mi, M. Liu, W. Lv and Y.-B. He, *Nano Energy*, 2022, **100**, 107470.

30. Q. Wu, M. Fang, S. Jiao, S. Li, S. Zhang, Z. Shen, S. Mao, J. Mao, J. Zhang, Y. Tan, K. Shen, J. Lv, W. Hu, Y. He and Y. Lu, *Nat. Commun.*, 2023, **14**, 6296.

31. S. Guo, S. Tan, J. Ma, L. Chen, K. Yang, Q. Zhu, Y. Ma, P. Shi, Y. Wei, X. An, Q. Ren, Y. Huang, Y. Zhu, Y. Cheng, W. Lv, T. Hou, M. Liu, Y. He, Q. Yang and F. Kang, *Energy Environ. Sci.*, 2024, **17**, 3797-3806.

32. H. Wang, H. Cheng, D. Li, F. Li, Y. Wei, K. Huang, B. Jiang, H. Xu and Y. Huang, *Adv. Energy Mater.*, 2023, **13**, 2204425.

33. M. Li, H. An, Y. Song, Q. Liu, J. Wang, H. Huo, S. Lou and J. Wang, *J. Am. Chem. Soc.*, 2023, **145**, 25632-25642.

34. J. Zheng, Z. Ju, B. Zhang, J. Nai, T. Liu, Y. Liu, Q. Xie, W. Zhang, Y. Wang and X. Tao, *J. Mater. Chem. A*, 2021, **9**, 10251-10259.

35. Y.-F. Huang, T. Gu, G. Rui, P. Shi, W. Fu, L. Chen, X. Liu, J. Zeng, B. Kang, Z. Yan, F. J. Stadler, L. Zhu, F. Kang and Y.-B. He, *Energy Environ. Sci.*, 2021, **14**, 6021-6029.

36. X. Pei, Y. Li, T. Ou, X. Liang, Y. Yang, E. Jia, Y. Tan and S. Guo, *Angew. Chem.*, 2022, **134**, e202205075.

37. Y. Xu, K. Wang, X. Zhang, Y. Ma, Q. Peng, Y. Gong, S. Yi, H. Guo, X. Zhang and X. Sun, *Adv. Energy Mater.*, 2023, **13**, 2204377.

38. J. F. Liu, Z. Y. Wu, F. J. Stadler and Y. F. Huang, *Angew. Chem. Int. Ed.*, 2023, **62**, e202300243.

39. T. Zhang, J. Li, X. Li, R. Wang, C. Wang, Z. Zhang and L. Yin, *Adv. Mater.*, 2022, **34**, 2205575.

40. P. Zhai, Z. Yang, Y. Wei, X. Guo and Y. Gong, *Adv. Energy Mater.*, 2022, **12**, 2200967.

41. Q. Zhou, X. Yang, X. Xiong, Q. Zhang, B. Peng, Y. Chen, Z. Wang, L. Fu and Y. Wu, *Adv. Energy Mater.*, 2022, **12**, 2201991.

42. K. Wen, C. Xin, S. Guan, X. Wu, S. He, C. Xue, S. Liu, Y. Shen, L. Li and C. W. Nan, *Adv. Mater.*, 2022, **34**, 2202143.

43. J. H. Park, M. J. Kwak, C. Hwang, K. N. Kang, N. Liu, J. H. Jang and B. A. Grzybowski, *Adv. Mater.*, 2021, **33**, e2101726.

44. D. Guo, D. B. Shinde, W. Shin, E. Abou-Hamad, A. H. Emwas, Z. Lai and A. Manthiram, *Adv. Mater.*, 2022, **34**, 2201410.

45. H. Wang, J. Song, K. Zhang, Q. Fang, Y. Zuo, T. Yang, Y. Yang, C. Gao, X. Wang and Q. Pang, *Energy Environ. Sci.*, 2022, **15**, 5149-5158.

46. P. Prakash, B. Fall, J. Aguirre, L. A. Sonnenberg, P. R. Chinnam, S. Chereddy, D. A.

Dikin, A. Venkatnathan, S. L. Wunder and M. J. Zdilla, *Nat. Mater.*, 2023, **22**, 627-635.

47. L. Tang, B. Chen, Z. Zhang, C. Ma, J. Chen, Y. Huang, F. Zhang, Q. Dong, G. Xue and D. Chen, *Nat. Commun.*, 2023, **14**, 2301.

48. X. Zhang, S. Wang, C. Xue, C. Xin, Y. Lin, Y. Shen, L. Li and C.-W. Nan, *Adv. Mater.*, 2019, **31**, 1806082.

49. L. Du, B. Zhang, W. Deng, Y. Cheng, L. Xu and L. Mai, *Adv. Energy Mater.*, 2022, **12**, 2200501.

50. Y. Ouyang, W. Gong, Q. Zhang, J. Wang, S. Guo, Y. Xiao, D. Li, C. Wang, X. Sun and C. Wang, *Adv. Mater.*, 2023, **35**, 2304685.

51. Q. Zhao, X. Liu, S. Stalin, K. Khan and L. A. Archer, *Nat. Energy*, 2019, **4**, 365-373.

52. J. Li, J. Qi, F. Jin, F. Zhang, L. Zheng, L. Tang, R. Huang, J. Xu, H. Chen and M. Liu, *Nat. Commun.*, 2022, **13**, 2031.